JGR Oceans

RESEARCH ARTICLE
10.1029/2021JC017760

The Daily-Resolved Southern Ocean Mixed Layer: Regional Contrasts Assessed Using Glider Observations

M. D. du Plessis[1,2], S. Swart[1,3], L. C. Biddle[1], I. S. Giddy[1,3], P. M. S. Monteiro[2], C. J. C. Reason[3], A. F. Thompson[4], and S.-A. Nicholson[2]

[1]Department of Marine Sciences, University of Gothenburg, Gothenburg, Sweden, [2]Southern Ocean Carbon-Climate Observatory, CSIR, Stellenbosch, South Africa, [3]Department of Oceanography, University of Cape Town, Cape Town, South Africa, [4]Environmental Science and Engineering, California Institute of Technology, Pasadena, CA, USA

Key Points:

- Regional glider missions reveal 1–10 day mixed layer variability in the Subantarctic, Polar, and sea-ice impacted Southern Ocean
- Surface heating drives buoyancy gain in all regions, while entrainment leads to buoyancy loss in the Subantarctic and Marginal Ice Zone
- In the Polar Frontal Zone, deep mixing by storms suppresses intraseasonal thermohaline variability

Supporting Information:

Supporting Information may be found in the online version of this article.

Correspondence to:

M. D. du Plessis,
marcel.du.plessis@gu.se

Citation:

du Plessis, M. D., Swart, S., Biddle, L. C., Giddy, I. S., Monteiro, P. M. S., Reason, C. J. C., et al. (2022). The daily-resolved Southern Ocean mixed layer: Regional contrasts assessed using glider observations. *Journal of Geophysical Research: Oceans*, *127*, e2021JC017760. https://doi.org/10.1029/2021JC017760

Received 16 JUL 2021
Accepted 7 MAR 2022

Abstract Water mass transformation in the Southern Ocean is vital for driving the large-scale overturning circulation, which transports heat from the surface to the ocean interior. Using profiling gliders, this study investigates the role of summertime buoyancy forcing and wind-driven processes on the intraseasonal (1–10 days) mixed layer thermohaline variability in three Southern Ocean regions southwest of Africa important for water mass transformation—the Subantarctic Zone (SAZ), Polar Frontal Zone (PFZ), and Marginal Ice Zone (MIZ). At intraseasonal time scales, heat flux was shown as the main driver of buoyancy gain in all regions. In the SAZ and MIZ, shallow mixed layers and strong stratification enhanced mixed layer buoyancy gain by trapping incoming heat, while buoyancy loss resulted primarily from the entrainment of cold, salty water from below. In the PFZ, rapid mixing linked to Southern Ocean storms set persistently deep mixed layers and suppressed mixed layer intraseasonal thermohaline variability. In the polar regions, lateral stirring of meltwater from seasonal sea-ice melt dominated daily mixed layer salinity variability. We propose that these meltwater fronts are advected to the PFZ during late summer, indicating the potential for seasonal sea-ice freshwater to impact a region where the upwelling limb of overturning circulation reaches the surface. This study reveals a regional dependence of how the mixed layer thermohaline properties respond to small spatiotemporal processes, emphasizing the importance of surface forcing occurring between 1 and 10 days on the mixed layer water mass transformation in the Southern Ocean.

Plain Language Summary The Southern Ocean extends from the cold and fresh polar waters near Antarctica to the warm and salty subtropics and is capped by a region called the mixed layer, where winds keep properties well mixed. Mixed layer waters play a key role in the Earth's climate by taking up heat from the atmosphere before being transported into the ocean interior, where they remain for centuries. The process by which heat leaves the mixed layer is poorly understood, but recent observations suggest that oceanic currents that vary on the scale of a few kilometers, that are not represented well in climate models, may dominate this exchange. Using autonomous ocean gliders at three locations from the northern to the southern Southern Ocean, we show that in the Subantarctic and sea-ice-impacted sea, shallow mixed layers lead to increased warming by trapping incoming heat from the atmosphere, while winds simultaneously mix up colder, saltier water from below. North of the sea-ice-impacted ocean, mixing by strong winds throughout the summer reduces mixed layer warming. Our findings show how mixed layer conditions within the Southern Ocean respond to daily weather variability, improving our understanding of how the ocean responds to the atmosphere above.

1. Introduction

The mixed layer is a boundary layer at the surface of the ocean that regulates the exchange of properties and energy between the atmosphere and the interior ocean. In the Southern Ocean, about 60% of the global ocean interior is upwelled to the mixed layer south of the Polar Front (DeVries & Primeau, 2011) where it is exposed to the atmosphere (Figure 1). Persistent westerly winds in the latitudes roughly spanning 60°–40°S (Patoux et al., 2009) support a northward Ekman transport at the ocean surface with Ekman convergence north of the Polar Front and Ekman divergence south of the Polar Front. Along the northern boundary of the Antarctic Circumpolar Current (ACC), surface ocean heat loss during winter results in deep mixed layers reaching up to 700 m (Dong et al., 2008; Tamsitt et al., 2020). These waters are transported into the ocean interior as Subantarctic Mode Water (SAMW) after subsequent shoaling of the mixed layer during summer. Further south, cold, and fresh surface waters influenced by sea-ice processes are transported northward across the Polar Front and

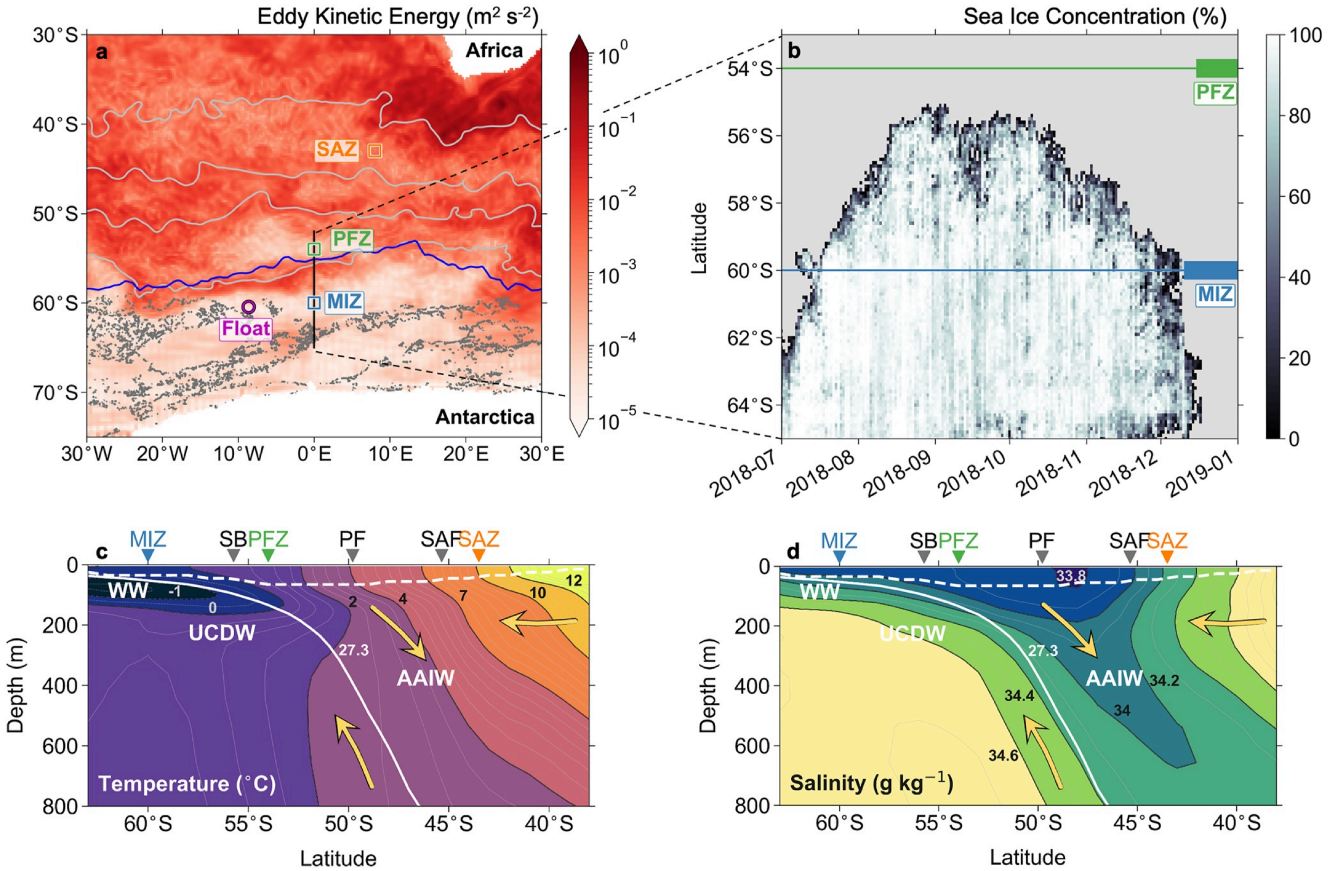

Figure 1. (a) The Atlantic Southern Ocean showing the mean eddy kinetic energy ($m^2\ s^{-2}$; derived from the AVISO gridded geostrophic velocities) for the duration of the study. Sea-ice concentration (%) from AMSR2 satellite (Spreen et al., 2008) shown as the blue (preceding winter sea-ice extent maximum, 5 September 2018) and gray (deployment of Marginal Ice Zone glider, 14 December 2018) contours. Glider locations and study sites for the Subantarctic Zone (SAZ, orange), Polar Frontal Zone (PFZ, green), and Marginal Ice Zone (MIZ, blue) are marked by colored squares. Location of a concurrently deployed Argo float located within the MIZ (60.45°S, 8.63°W) shown by the magenta circle. The mean Southern Ocean fronts (defined as in Swart et al. [2010]) are shown by the light gray lines. From north to south, these are the Subtropical Front (STF), Subantarctic Front (SAF), Polar Front (PF), and Southern Boundary (SB). (b) Hovmöller of sea-ice concentration (%) along 0°E marked by the vertical black line in (a). Colored blocks show the date and latitude of the PFZ (green) and MIZ (blue) glider campaigns. Meridional sections showing the summer (DJF) climatological (c) temperature and (d) salinity averaged zonally across 5°W and 10°E using EN4.2.1 data (Good et al., 2013). Marked on (c) and (d) are black contours labeled for temperature (°C) and salinity (g kg^{-1}) respectively, the mixed layer depth (MLD; dashed white line), the 27.3 kg m^{-3} isopycnal (solid white line), indicating the upper bound of the Upper Circumpolar Deep Water (UCDW), gray markers show the location of the SAF, PF, and SB fronts, colored arrows show the latitudinal position of the glider deployments and yellow arrows indicate the general flow direction of the residual overturning circulation. Water mass locations indicated in white text are Winter Water (WW), UCDW, and Antarctic Intermediate Water (AAIW).

carried into the interior along density surfaces as Antarctic Intermediate Water (AAIW). The transport of these surface waters toward the ocean interior indicates that the mechanisms which alter the mixed layer properties of the Southern Ocean ultimately determine the role of the long-term oceanic storage of heat and freshwater. Using a data assimilating model, Abernathey et al. (2016) showed that the Lagrangian, time-mean water mass formation rate of AAIW is dominated by upper ocean buoyancy gain through ice melt and precipitation, but is lower than expected due to buoyancy loss by mixing processes. SAMW formation is driven by both surface warming and freshening, underlining the importance of constraining air-sea flux processes for mode water formation. These water mass transformation processes that occur between the upwelling of deep water and subduction into the ocean interior (Marshall & Speer, 2012) has climatic implications through the draw-down of heat and carbon into the ocean interior (Meredith et al., 2019; Sallée, 2018).

Water mass transformation can be understood through the variability of mixed layer thermohaline properties, which occur at different rates through the interactions of heat and freshwater fluxes. The seasonal cycle is one of the dominant modes of variability of the Southern Ocean mixed layer and so examining what drives the seasonal cycle of mixed layer temperature (T_m) and salinity (S_m) provides important insight into the physics that

lead to water mass transformation. In ice-impacted regions, the freshwater flux, driven primarily by the annual advance and melt of sea-ice, dominates the heat flux contribution to net buoyancy by a factor of 5 (Pellichero et al., 2017, 2018). In ice-free regions, the seasonal cycle in heat flux dominates stratification, with entrainment and Ekman advection, which act to cool the mixed layer, being of secondary importance (Dong et al., 2007; Pellichero et al., 2017).

Intraseasonal (1–10 days) dynamics may also be important for driving mixed layer thermohaline variability. Vivier et al. (2010) used a two-dimensional diagnostic model to show that heat flux and Ekman advection account for up to 70% of the daily temperature variance across the Southern Ocean (south of 30°S), while eddy heat diffusion is argued to provide the same order of variability in regions of strong lateral temperature gradients such as along the Subantarctic Front and downstream of the Agulhas retroflection (Sallée et al., 2006, 2008). Mesoscale eddies have been shown to alter the turbulent heat flux by 10–20 W m^{-2} through modifying the air-sea temperature gradient (Villas Bôas et al., 2015), while eddy advection can supplement up to 40% of the heat gained by air-sea heat fluxes (Tamsitt et al., 2016). However, due to the logistical challenges of acquiring in situ observations in remote regions, studies that investigate the role of surface buoyancy forcing and wind-driven processes on the basin-wide variability T_m and S_m have been limited to using 1°, monthly climatological data products, which apply lateral and temporal smoothing techniques that suppress the effect of (sub)mesoscale eddies and synoptic weather events (Dong et al., 2007; Pellichero et al., 2017, 2018; Ren et al., 2011).

Southern Ocean storms, associated with a frequency of 4–9 days (Carranza & Gille, 2015; Swart et al., 2015), provide a key scale of variability to mixed layer dynamics. Storms, with wind stresses frequently more than 0.8 N m^{-2}, provide significant energy input into the surface ocean (Lin et al., 2018; Yuan et al., 2009), increasing the near-surface diffusive mixing to the mixed layer base that entrains denser water from below (Forryan et al., 2015; Jouanno et al., 2016). Whitt et al. (2019) assessed the role of subseasonal wind variability on the mixed layer depth (MLD) in a modeling study by comparing two simulations that only differed by applying a 60-day low-pass filter to the wind. Their study found that the simulation which included the higher frequency winds (including storms) had a global mean MLD deeper by 25% (see their Figure 15). In the sea-ice-impacted regions of the Southern Ocean, these intraseasonal winds are shown to alter the phasing of the seasonal cycle of MLDs. Such modifications are likely to impact water mass transformation in these regions, yet the associated storm-driven mechanisms remain unknown.

Furthermore, submesoscale (0.1–10 km) processes associated with fronts, eddies, and meanders can modify this framework by enhancing mixing through lateral cross-frontal advection (du Plessis et al., 2019; Whitt & Taylor, 2017) or suppressing mixing by restratifying the upper ocean through a vertical buoyancy flux associated with mixed layer baroclinic instability (MLI; Boccaletti et al., 2007; Fox-Kemper et al., 2008). Su et al. (2018) propose that the vertical heat transport associated with MLIs increase the mean state of mixed layer temperature by 0.06–0.3°C, while producing an upward annual mean heat flux anomaly of 4–10 W m^{-2} in midlatitudes. The small spatial scales and rapid temporal scales (hours to days) of submesoscale flows make in situ observations of their impact on the mixed layer in the Southern Ocean difficult. Nevertheless, there is now increasing evidence that submesoscale flows are energized in frontal regions of the ACC (Adams et al., 2017; Bachman et al., 2017; du Plessis et al., 2017, 2019), at topographic features (Dove et al., 2021; Rosso et al., 2015; Viglione et al., 2018) and sea-ice melt regions (Biddle & Swart, 2020; Giddy et al., 2021; Swart et al., 2020). Even so, understanding the role of submesoscale flows on mixed layer thermohaline variability at the spatiotemporal scales at which they vary remains a significant challenge.

In this study, we address the role of atmospheric forcing (wind and buoyancy forcing) on the mixed layer temperature and salinity variability at daily time scales in the Southern Ocean. We use data from a multiglider observational experiment designed to concurrently sample three regions where such mixed layer variability is thought to play an important role for water mass modifications (Figure 1): the Subantarctic Zone (SAZ), Polar Frontal Zone (PFZ), and Marginal Ice Zone (MIZ). A daily T_m and S_m budget is determined for each site to elucidate the key processes at play. We further provide a scaling for the role of lateral submesoscale processes which enhance the variability of the MLD and stratification. In Section 2, we describe the methodology and data sets used. In Section 3, we describe the results, while in Section 4, we discuss the findings of this work within the broader literature and the potential consequences of the assumptions that we used in this study.

2. Methods

2.1. Field Sites and Glider Data Sets

We used data collected from two Kongsberg Seagliders and a Teledyne Webb Slocum G2 Slocum, which were deployed as a part of the Robotic Observations and Modeling of the Marginal Ice Zone (ROAM-MIZ) and SOSCEx-STORM2 as part of the Southern Ocean Seasonal Cycle Experiment (Swart et al., 2012). Furthest north, a Seaglider was deployed in the Subantarctic region southwest of Africa (43.5°S, 8°E) characterized by intense mesoscale activity of the subtropical western boundary current (Agulhas Rings) and the ACC (Faure et al., 2011; Figure 1). The second Seaglider sampled in the northeastern Weddell Sea (60°S, 0°E). At the outset of the experiment, the glider was deployed in a region consistent with traditional definitions of the MIZ, a low-concentrated sea-ice regime between the open ocean and pack ice, with highly variable conditions that can be impacted by waves and swell. While we retain MIZ as a label for this region, following Swart et al. (2020) and Giddy et al. (2021), we emphasize that during most of the glider deployment, the region is better described as part of the seasonal ice zone, since it was ice-free. Finally, a Slocum glider sampled in the Polar upwelling region along the meridian north of the maximum winter sea-ice edge (54°S, 0°E; Figure 1a).

The two Seagliders and Slocum glider were equipped with conductivity (salinity) and temperature sensors that provided continuous measurements as the gliders profiled the water column. The sampling frequencies of CT sensors were 5 s for the Seagliders and 1 s for the Slocum, resulting in a vertical sampling interval ranging between 0.2–1.5 m (Seagliders) and 0.05–0.2 m (Slocum). The raw Seaglider data files underwent initial processing to adjust the temperature for a first-order thermistor-response lag and correct salinity for thermal-inertia effects following the methods of Garau et al. (2011). The Slocum data set was processed with the GEOMAR MATLAB toolbox, which includes the removal of minor thermal-lag errors. Postprocessing of all gliders was performed using the GliderTools Python toolbox (Gregor et al., 2019). This involved the classification and removal of erroneous data points in temperature and salinity, defined as values larger than a 5-point rolling standard deviation. The temperature and salinity profiles were then linearly interpolated to a depth interval of 5 m. Temperature and salinity were converted to conservative temperature and absolute salinity using the Gibbs Seawater Toolbox (McDougall & Barker, 2011).

The MLD was defined as the depth to which properties of temperature, salinity, and density are vertically homogeneous from the surface ocean. As both temperature and salinity can determine upper ocean stratification, we determined MLD following the density threshold criteria of 0.03 kg m^{-3} from a reference depth of 10 m (de Boyer Montégut et al., 2004), which has shown to be robust in the Southern Ocean (Dong et al., 2008; Holte & Talley, 2009). Next, we obtained T_m and S_m by taking the mean temperature and salinity between 5 m below the surface and 5 m above the MLD. By using this method, we removed temperature and/or salinity gradients induced by surface skin-layer processes as well as any residual thermal-lag issues which may still exist within the pycnocline.

The gliders were deployed on the 10, 13, and 14 December 2018 and retrieved on the 12, 9, and 26 March 2019, resulting in 93, 81, and 101 days of sampling for the SAZ, PFZ, and MIZ, respectively (Figure 2). Different sampling strategies were employed for each glider: the SAZ glider remained in a "virtual mooring" mode, only once transecting about 20 km southward on Yearday 15 (Figures 2a and 2f); the PFZ glider performed repeat north-south transects about 12 km in length (Figures 2b and 2f); and the MIZ performed a "bow-tie" pattern of roughly 20 km in length (Figures 2c and 2f), with two north-south mesoscale transects (185 and 120 km) in the beginning and middle of the experiment. Although all three gliders were piloted to understand the role of small-scale, high-frequency mixed layer processes. The SAZ glider was kept in the Eulerian "mooring mode" to understand the role of one-dimensional mixed layer processes. The repeat sections of the PFZ glider were done to follow the path of a concurrent Wave Glider deployment, and the bow-tie performed by the MIZ glider was done to capture the lateral mixed layer gradients induced by sea-ice processes and investigate their role on mixed layer variability.

The MIZ glider was deployed only 4 days after the local sea-ice completely melted, while the PFZ glider was ∼120 km north of the previous winter's maximum sea-ice extent, which occurred on 5 September 2018 (Figure 1b). An under-ice Argo float sampled near the MIZ glider (60.45°S, 8.63°W), providing a temperature and salinity profile of the upper 2,000 m every 10 days. The evolution of the salinity profile showed that S_m had been decreasing since mid-November and so indicating the beginning of sea-ice melt (Figure 3). Between

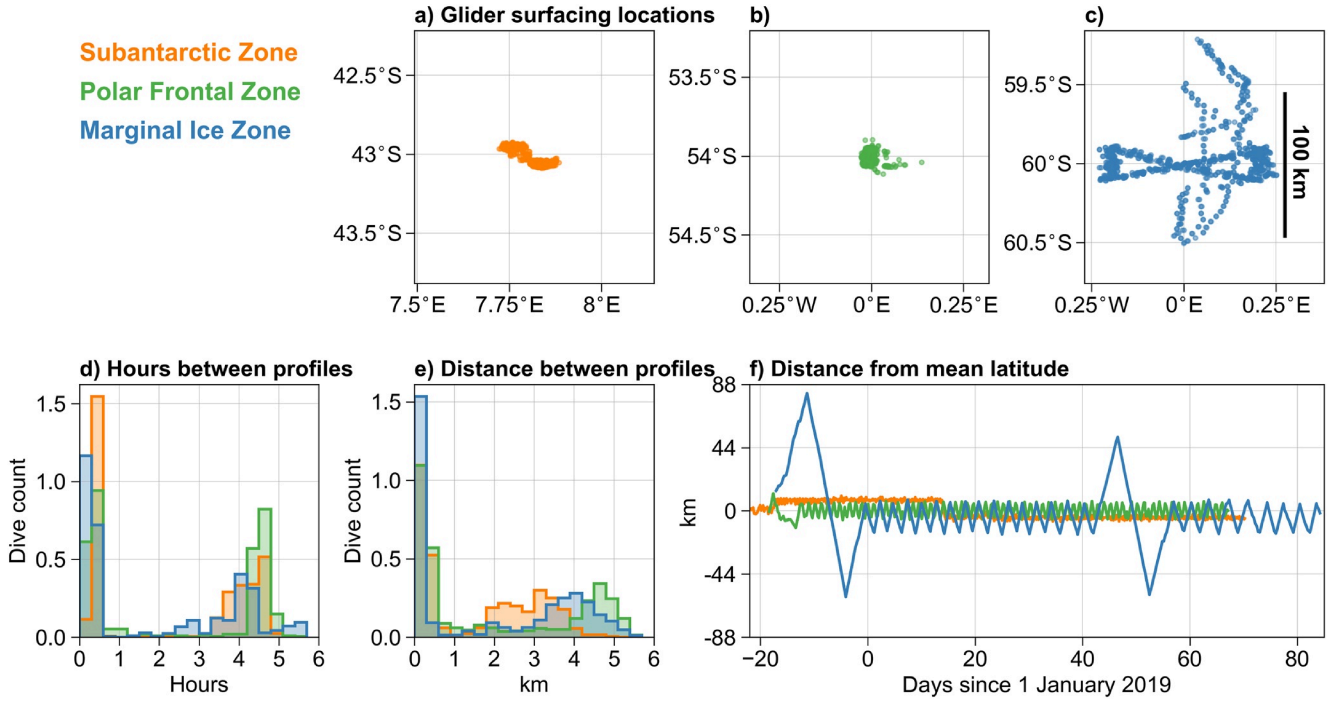

Figure 2. Glider surfacing locations for the (a) Subantarctic Zone (SAZ), (b) Polar Frontal Zone (PFZ), and (c) Marginal Ice Zone (MIZ). Dots indicate the location of the glider directly after the surfacing of a climb and before the following dive, indicating the locations of where the glider sampled the mixed layer. Note the *y*-limits are of equivalent meridional distance. A statistical distribution of the (d) temporal and (e) spatial resolution of the glider surfacing locations. Note that orange, green, and blue histograms are for the SAZ, PFZ, and MIZ, respectively. (f) The time series of the meridional distance covered for each region.

mid-November and the deployment of the MIZ glider (14 December), S_m had freshened by ~0.2 g kg^{-1} and the mixed layer had restratified from 110 to 50 m. T_m increased by ~0.3°C from the in situ freezing temperature by the time of complete sea-ice melt (13 December), increasing by a further ~0.7°C 10 days later. As such, the MIZ glider provides a unique perspective on the evolution of the mixed layer thermohaline properties in response to the restratification induced by seasonal sea-ice melt.

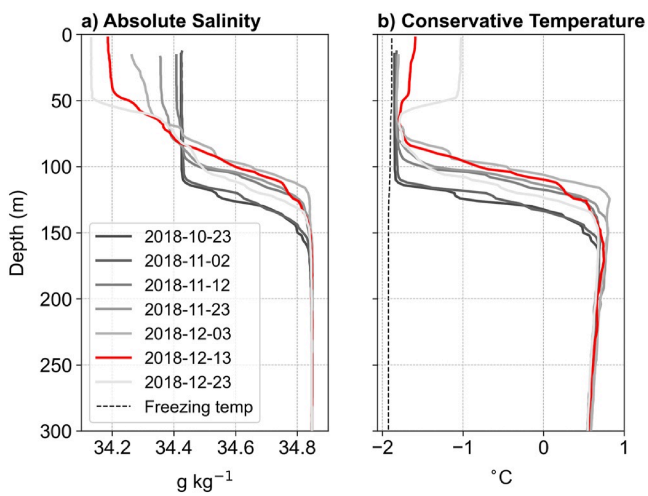

Figure 3. Upper ocean profiles of (a) absolute salinity (g kg^{-1}) and (b) conservative temperature (°C) from an Argo float located within the Marginal Ice Zone (MIZ; 60.45°S, 8.63°W) between 23 October 2018 and 23 December 2018 showing the progression of the upper ocean thermohaline properties prior to, during and post sea-ice melt at a location nearby the MIZ glider. The gray lines are colored dark to light as the season progresses from spring to summer, the red line is the profile obtained 1 day prior to the MIZ glider deployment while the black dashed line in (b) shows the in situ freezing point temperature.

We note that this study aims to analyze the temporal variability of the mixed layer thermohaline properties and treats the glider data in an Eulerian sense. However, we must consider that by a function of their design, the gliders move laterally during dive cycles (Figure 2f) and so consecutive glider profiles potentially transect across lateral temperature and salinity gradients. As such, the gliders may observe changes in T_m and S_m that are related to spatial processes, such as submesoscale gradients, rather than temporal processes such as heat and freshwater fluxes. Furthermore, the different sampling approaches from the gliders will result in different contributions from mesoscale variability and seasonality. For example, the two mesoscale transects performed by the MIZ glider will likely show T_m and S_m variability associated with spatial gradients in addition to the temporal variability.

We expect that the contribution of lateral temperature and salinity gradients to the glider-observed daily changes in T_m and S_m will increase with decreasing internal Rossby radius of deformation ($L_f = Nh_m/f$, where N is the buoyancy frequency, h_m is the MLD, and f the Coriolis frequency) as the scale at which ageostrophic fronts develop become less than the lateral displacement of the glider dive cycle. The mean Rossby radius of deformation at the three sites were comparable (L_f = 2.1, 2.0, and 1.9 km) with the mean spatial resolution of the gliders (1.6 ± 1.4, 2.0 ± 2.0, and 1.9 ± 2.0 km), which also have

a mean temporal resolution of 2.3 ± 1.9, 2.5 ± 2.1, and 2.5 ± 2.3 hr. The similar length scales of L_f and lateral glider displacement between dives suggests that the gliders may have transected through submesoscale gradients during dives. In regions of enhanced lateral gradients of T_m and S_m, therefore, our Eulerian approach may include a spatial bias.

2.2. Mixed Layer Temperature and Salinity Budget

To investigate the contributions of air-sea heat and freshwater fluxes, Ekman advection and vertical entrainment to the tendency of T_m and S_m, we estimated a simplified temperature and salinity budget

$$\frac{T_m}{\partial t} = \frac{Q_{net}}{\rho_0 C_p h_m} - v_{Ek}\frac{\partial T_m}{\partial y} - \frac{w_e \Delta T_m}{h_m} + R_T, \quad (1)$$

$$\frac{S_m}{\partial t} = \frac{(E-P)S_m}{h_m} - v_{Ek}\frac{\partial S_m}{\partial y} - \frac{w_e \Delta S_m}{h_m} + R_S. \quad (2)$$

In Equations 1 and 2, the left-hand side corresponds to the tendency terms for temperature (°C s^{-1}) and salinity (g kg^{-1} s^{-1}), respectively, while Q_{net} is the net surface heat flux (W m^{-2}), ρ_0 is a reference density (1,025 kg m^{-3}), C_p is the specific heat capacity of seawater (3,850 J kg^{-1} K^{-1}), v_{Ek} is the meridional component of the Ekman velocity (m s^{-1}) and defined in Section 2.2.4, w_e is the entrainment velocity (m s^{-1}), E and P are evaporation and precipitation in m s^{-1}, while ΔT_m and ΔS_m correspond to the temperature and salinity difference between the base of the mixed layer and 15 m below the MLD. The choice of 15 m was based on the sensitivity analysis by Ren et al. (2011). R_T and R_S represent a temperature and salinity residual term accounting for the processes not represented in Equations 1 and 2, such as vertical and horizontal diffusion, geostrophic and vertical advection as well as the uncertainties in the calculated terms, such as in the reanalysis data.

2.2.1. Air-Sea Fluxes: ERA5 Reanalysis

The air-sea fluxes of heat, freshwater, and momentum required in Equations 1 and 2 were extracted from the 1-hr, 0.25° resolution ERA5 reanalysis of the European Centre for Medium Range Weather Forecasts (Hersbach et al., 2020). The variables used in this study include the 10 m above sea level u and v components of the wind speed, the shortwave (Q_{sw}) and longwave (Q_{lw}) radiative heat fluxes, the sensible (Q_{sens}) and latent (Q_{lat}) turbulent heat fluxes, and evaporation (E) and precipitation (P). Using the above variables, we determine the wind stress following Large and Pond (1981); $\tau = \rho a C_D U_{10}^2$, where ρ_a is the density of air, U_{10} is the wind speed 10 m above sea level, and C_D is the drag coefficient. The drag coefficient has a constant value of 1.15×10^{-3} for $U_{10} < 11$ m s^{-1}, but varies with the wind as $4.9 \times 10^{-4} + 6.5 \times 10^{-5} \times U_{10}$ for $U_{10} > 11$ m s^{-1}. The net surface heat flux is determined as $Q_{net} = Q_{sw} + Q_{lw} + Q_{sens} + Q_{lat}$. Positive heat and freshwater fluxes indicate the ocean gaining buoyancy (Figure 4). A description of why ERA5 is chosen and the potential uncertainties associated with using reanalysis data in this study are discussed in Section 4.4.

2.2.2. Mixing Layer Depth Estimation

The mixing layer depth (XLD) represents the depth of vertical mixing from local forcing mechanisms (including storms) and can thus be associated with the wind-driven advective layer. The XLD is different from the MLD since it represents the active mixing processes while the MLD represents the net effect of previous mixing events on the vertical structure of the water column. We determined the XLD following (Brainerd & Gregg, 1995) as the depth from the surface where the dissipation rate of turbulent kinetic energy (ϵ) first drops below 10^{-8} m^{-2} s^{-3}. The measurements of ϵ were derived from shear probes on a Rocklands microstructure profiler deployed on the PFZ Slocum glider. See Nicholson et al. (2022) for details. Nicholson et al. (2022) showed that the XLD showed a strong dependence on the friction velocity, $u* = \sqrt{\tau/\rho_0}$ ($r^2 = 0.75$, their Figure S5), and so an estimated XLD, represented as h_x, was be determined from $u*$ with a root mean error of 12 m (both the true and estimated XLD have a mean of 59 m). We applied this relationship to determine h_x for the SAZ and MIZ. We chose not to use other mixing depth estimates such as that determined by Pollard et al. (1973) and the Ekman layer depth as we found those depths were too shallow to explain the variability of the observed MLD (Figure S1).

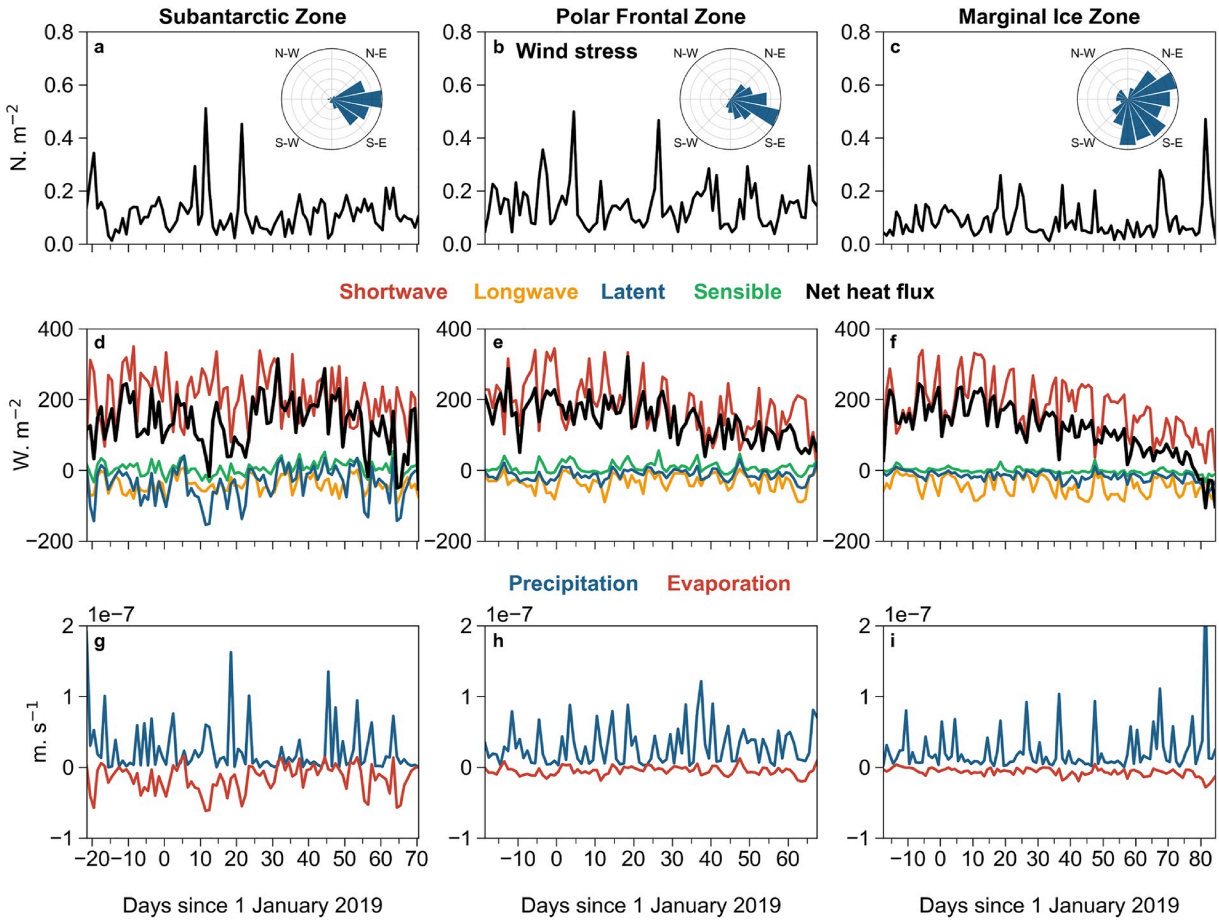

Figure 4. ERA5 air-sea forcing terms linearly interpolated to each glider surfacing location and averaged to a daily resolution for the Subantarctic Zone (a, d, g), Polar Frontal Zone (b, e, h), and Marginal Ice Zone (c, f, i). (a–c) Wind stress (N m^{-2}) as black lines, wind rose insets show wind direction. (d–f) Net surface heat flux (Q_{net}, black line), including the four components of shortwave (Q_{sw}, red line), longwave (Q_{lw}, orange line), latent (Q_{lat}, blue line), sensible (Q_{sens}, green line) heat fluxes with units of W m^{-2}. (g–i) Evaporation (red line) and precipitation (blue line) with units of m s^{-1}.

2.2.3. Entrainment

Entrainment was considered here as an irreversible flux of temperature and salinity into the mixed layer from below as a result of the active mixing layer exceeding the mixed layer (i.e., XLD > MLD). The rate that entrainment takes place was given by

$$w_e = \mathcal{H}\left(\frac{\partial h_m}{\partial t}\right). \tag{3}$$

Using x = XLD/MLD

$$\mathcal{H}(x) = \begin{cases} 1, \text{if } \times \geq 1 \\ 0, \text{if } \times \leq 1. \end{cases} \tag{4}$$

In addition, the entrainment term was only nonzero if the MLD, as determined from the glider data, deepened from 1 day to the next.

2.2.4. Ekman Advection

Ekman transport was be computed from wind stress as

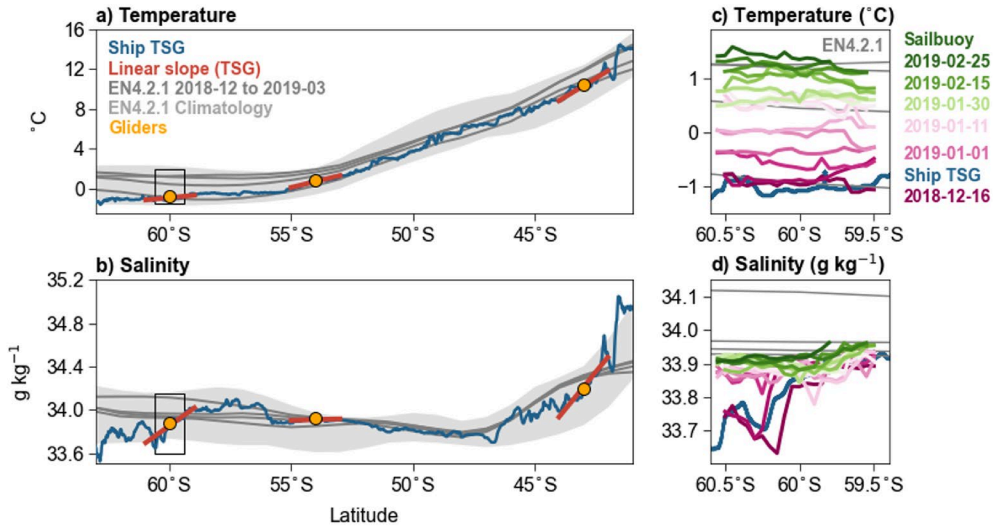

Figure 5. Meridional distribution of (a) temperature (°C) and (b) salinity (g kg^{-1}). Shipboard thermosalinograph (TSG) data at 6-m depth taken during the deployment cruise is indicated by the blue line, the monthly interpolated 5 m temperature and salinity from EN4.2.1 between December 2018 and March 2019 shown as gray lines. Gray shading indicates the range of all December to March months between 2002 and 2020. Red lines represent mesoscale temperature and salinity gradients (slope) calculated from the TSG data between 1° north and south of each glider location. Orange dots mark the latitudinal positions of the gliders, from the right (north) to left (south) representing the Subantarctic Zone, Polar Frontal Zone, and Marginal Ice Zone. Black box insets in (a) and (b) correspond to subplots (c) and (d), which show the ship TSG and EN4.2.1 monthly values as in (a) and (b), as well as the summer progression (pink to green) of surface temperature and salinity obtained from repeat Sailbuoy transects (see Swart et al., 2020).

$$v_{Ek} = \frac{\tau^x}{\rho_0 f h_x}. \tag{5}$$

where τ^x is the zonal component of the wind stress and ρ_0 is a reference potential density of 1,025 kg m^{-3}. Ekman theory assumes that the time scales for Ekman transport to spin-up are comparable to or longer than the inertial period ($2\pi/f$). With the local inertial periods at 17.4, 14.8, and 13.8 hr, a 24-hr rolling mean was applied to τ^x. We assumed that the meridional component of the Ekman advection was considerably larger than the zonal given that the wind direction is predominantly westerly across at our study sites (Figures 4a–4c).

2.2.5. Lateral Temperature and Salinity Gradients

We obtained $\partial(T_m, S_m)/\partial y$ for the SAZ and PFZ as the mean property gradient over 1° latitude (~110 km) north and south of each glider location from a shipboard thermosalinograph (TSG) mounted to the hull (6-m depth) of the vessel during the glider deployment voyage. For the MIZ, we used surface temperature and salinity obtained from a concurrently deployed Offshore Sensing Sailbuoy, an autonomous surface vehicle that measured temperature and salinity at a depth of 1 m below the sea surface. The Sailbuoy performed repeat mesoscale transects between 59.5°S and 60.5°S (along 0°E) from 14 December 2018 to the end of February (Figures 5c and 5d, see Swart et al. (2020) for details). The horizontal resolution of the TSG and Sailbuoy was 28 ± 55 and 493 ± 237 m, respectively (Figure 5). Note that to determine the Ekman advection term for the MIZ region, we used 18 Sailbuoy transects performed over the location of the Seaglider, while for the SAZ and PFZ, we used only a single transect taken from the TSG during the deployment voyage.

3. Results

3.1. Mixed Layer Variability From Gliders

To understand the intraseasonal variability of the MLD within each region, we first determined the upper ocean vertical stratification (N^2, Figure 6) calculated as

$$N^2 = \frac{-g}{\rho_0}\frac{\partial \rho}{\partial z}, \tag{6}$$

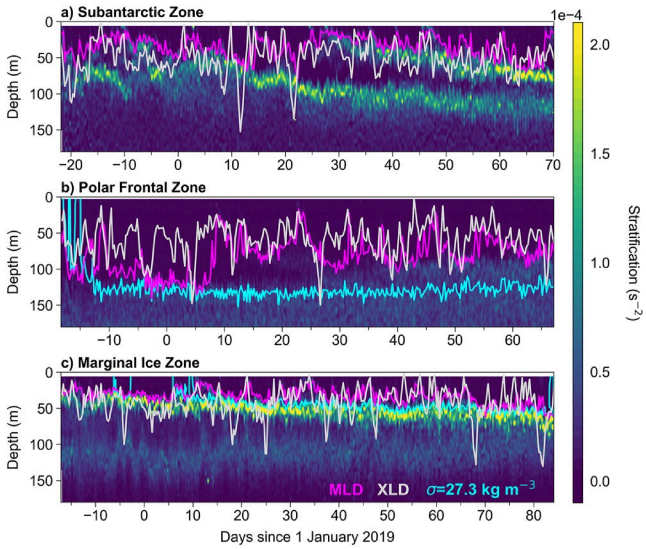

Figure 6. Vertical sections of the glider stratification (N^2, Equation 6) for the (a) Subantarctic Zone, (b) Polar Frontal Zone, and (c) Marginal Ice Zone. Magenta line shows the mixed layer depth (MLD), gray line is the mixing layer depth (XLD), and the cyan line the 27.3 kg m^{-3} potential density anomaly contour indicating the upper bound of Upper Circumpolar Deep Water.

where g is the gravitational acceleration and ρ_0 is a reference density taken as 1,025 kg m^{-3}.

The MLD values in the SAZ (mean ± standard deviation: 45 ± 15 m) and MIZ (41 ± 8 m) were much shallower than the PFZ (105 ± 17 m). This is likely due to the contrast of stratification at the base of the mixed layer, with the mean N^2 between the MLD and 15 m below $\left(N^2_{MLD}\right)$ for all profiles in the PFZ (0.27×10^{-4} s^{-2}) being less than half the value in the SAZ (0.64×10^{-4} s^{-2}) and MIZ (1.1×10^{-4} s^{-2}). Further, intraseasonal variability—indicated by the standard deviation of N^2_{MLD}—was comparable in the SAZ (3.7×10^{-5} s^{-2}) and MIZ (3.8×10^{-5} s^{-2}) but about four times lower in the PFZ (1.0×10^{-5} s^{-2}). In the SAZ, the largest MLD variations were characterized by two restratification events occurring on Yearday 24 and 46, where the MLD shoaled by 72 and 35 m within 30 and 42 hr, respectively. Similarly, during strong wind periods as seen on Yearday −4 and 48 (τ = 0.16 and 0.21 N m^{-2}), with XLD > MLD, the mixed layer deepened again, increasing by 34 and 42 m within 24 and 72 hr, respectively. In contrast, the MLD in the PFZ shoaled only once, from 141 to 65 m over 12 days between Yearday 13 and 25, despite two strong wind events (τ = 0.25 N m^{-2} and 0.29 N m^{-2}) on Yearday 14 and 18. On Yearday 26, the strongest winds of the summer (τ > 0.7 N m^{-2}) resulted in the XLD reaching 149 m (deepest of the summer), which deepened the mixed layer again. However, the mean state of the MLD was altered from 125 ± 8 m before the restratification event (Yearday −18 to 26) to 93 ± 9 m after (Yearday 26 to 68). In the MIZ, the recently melted sea-ice shoaled the MLD to 50 m. The wind stress exceeded 0.1 N m^{-2} every 2–5 days (Figure 4c) and the XLD regularly exceeded the MLD, a gradual deepening of the mixed layer was observed and reached a maximum of 67 m by Yearday 83, approximately 3 months after sea-ice melted. However, the MLD restratified during periods of sustained low winds (τ < 0.1 N m^{-2}, e.g., from Yearday 9 to 12 by 29 m and from Yearday 31 to 36 by 31 m).

3.2. Daily Variations in the Mixed Layer Thermohaline Properties

Next, we determined the role of air-sea heat and freshwater fluxes, Ekman advection, and entrainment on the daily thermohaline variations between the three regions (Figures 7 and 8).

3.2.1. Temperature

The mixed layer temperature in all regions increased over the summer at a rate indicated by the daily mean and standard deviation of 0.04 ± 0.08, 0.02 ± 0.01, and 0.07 ± 0.04°C day^{-1} in the SAZ, PFZ, and MIZ respectively (Figures 7a–7c). Notable differences exist in the mean warming rates, where the PFZ had a 71% lower warming rate than the MIZ despite a larger mean net surface heat flux (135 ± 74, 146 ± 58, and 117 ± 72 W m^{-2} for the three regions, respectively). These differences are linked to the processes that enhance or reduce mixed layer warming at times scales of 1–10 days, where T_m varied by up to 0.1°C day^{-1} in the PFZ and 0.2°C day^{-1} in the SAZ and MIZ (Figures 7h and 7i).

We determined the individual terms in the mixed layer temperature budget (Equation 1) to understand the key drivers of the observed intraseasonal variability (Figures 7e and 7f). At daily time scales, the sum of the budget terms accounted for about half of the glider-observed mixed layer temperature variability (r^2 = 0.55, 0.43, and 0.59 for SAZ, PFZ, and MIZ, respectively, Figures 7h and 7i). Furthermore, the qualitative agreement between the net terms and the observations allowed us to contrast the key processes of intraseasonal T_m variability between the three sites that are expanded on below.

In the absence of any other processes, net surface heat fluxes would cause a warming of the mixed layer at a rate of 0.08 ± 0.06, 0.03 ± 0.01, and 0.07 ± 0.05°C day^{-1} for the SAZ, PFZ, and MIZ, respectively (Figures 7d–7f). Notably, the relatively low mean rate of warming by heat flux in the PFZ (less than half of the other two zones) occurred despite receiving the largest mean heat flux, exceeding 0.06°C day^{-1} only once on Yearday 19 (during the restratification event). Meanwhile, the largest individual warming days of 0.29°C day^{-1} were in the SAZ

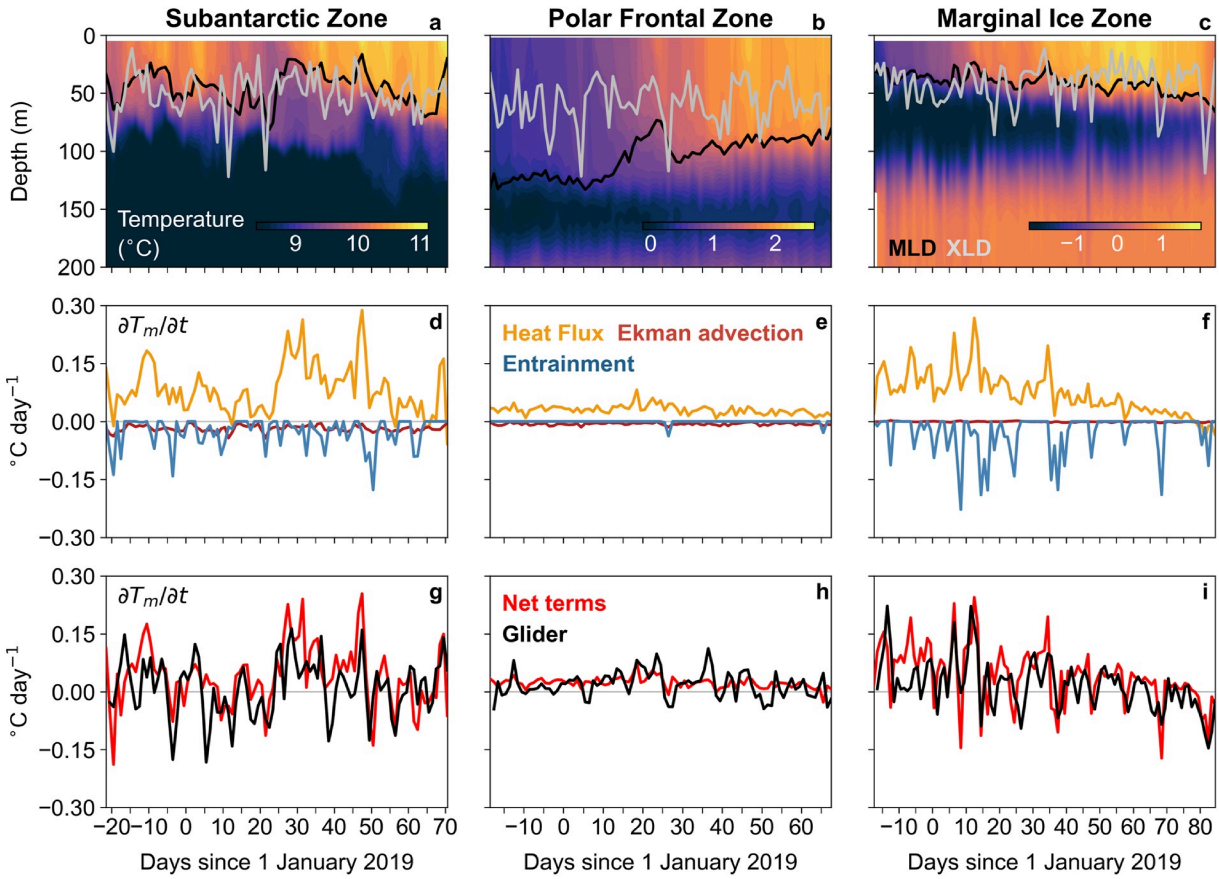

Figure 7. (a–c) Vertical sections of temperature (°C) measured by the gliders for the Subantarctic Zone, Polar Frontal Zone, and Marginal Ice Zone, respectively. Lines indicate the mixed layer depth (MLD; black) and mixing layer depth (gray). Note the colorbar limits vary but are scaled to a range of 2.5°C. (d–f) Daily T_m change ($\partial T_m/\partial t$, °C day^{-1}) resulting from heat flux (orange), entrainment (blue), and Ekman advection (red) as described in Equation 1. (g–i) Red lines indicate the daily T_m change determined from the sum of the budget terms in Equation 1 (lines in d–f), while black line is the observed daily T_m change determined from the glider data in units of °C day^{-1}.

(Yearday 48) and MIZ (Yearday 13; Figures 4d and 4f). These warming days occurred during the shallowest MLDs of the summer (<30 m), while deep mixing events (XLD >100 m) led to suppressed warming or even cooling in the summer.

In the SAZ, the TSG mesoscale meridional temperature gradient (−0.013°C km^{-1}) was more than twice as strong as the PFZ (−0.0054°C km^{-1}) and an order of magnitude stronger than in the MIZ (mean Sailbuoy mesoscale gradient of -0.0013 ± 0.0011°C km^{-1}). In the MIZ, strong westerly winds (mean $\tau^x = 0.1 \pm 0.1$ N m^{-2}) which blew over this gradient led to a northward Ekman flow that cooled the mixed layer at a mean rate of −0.017°C day^{-1} (Figure 7d). Further cooling was provided by entrainment during enhanced storm-driven (>0.2 N m^{-2}) mixing events (e.g., on Yearday 12 and 37, Figure 7a) at a rate of between −0.06 and −0.18°C day^{-1}.

In the MIZ, the dominant mixed layer cooling process was entrainment of Winter Water (WW), with a negligible contribution from the advective terms (Figure 7f). The vertical flux of warmer mixed layer waters into the WW resulted in a thinning and warming of WW from ∼−1.6°C in early summer to ∼−0.5°C 3 months later. Over the summer, six entrainment events (Yearday −4, 17, 25, 38, 68, and 82) associated with intense winds (>0.3 N m^{-2}) led to T_m cooling of about 0.2°C day^{-1}.

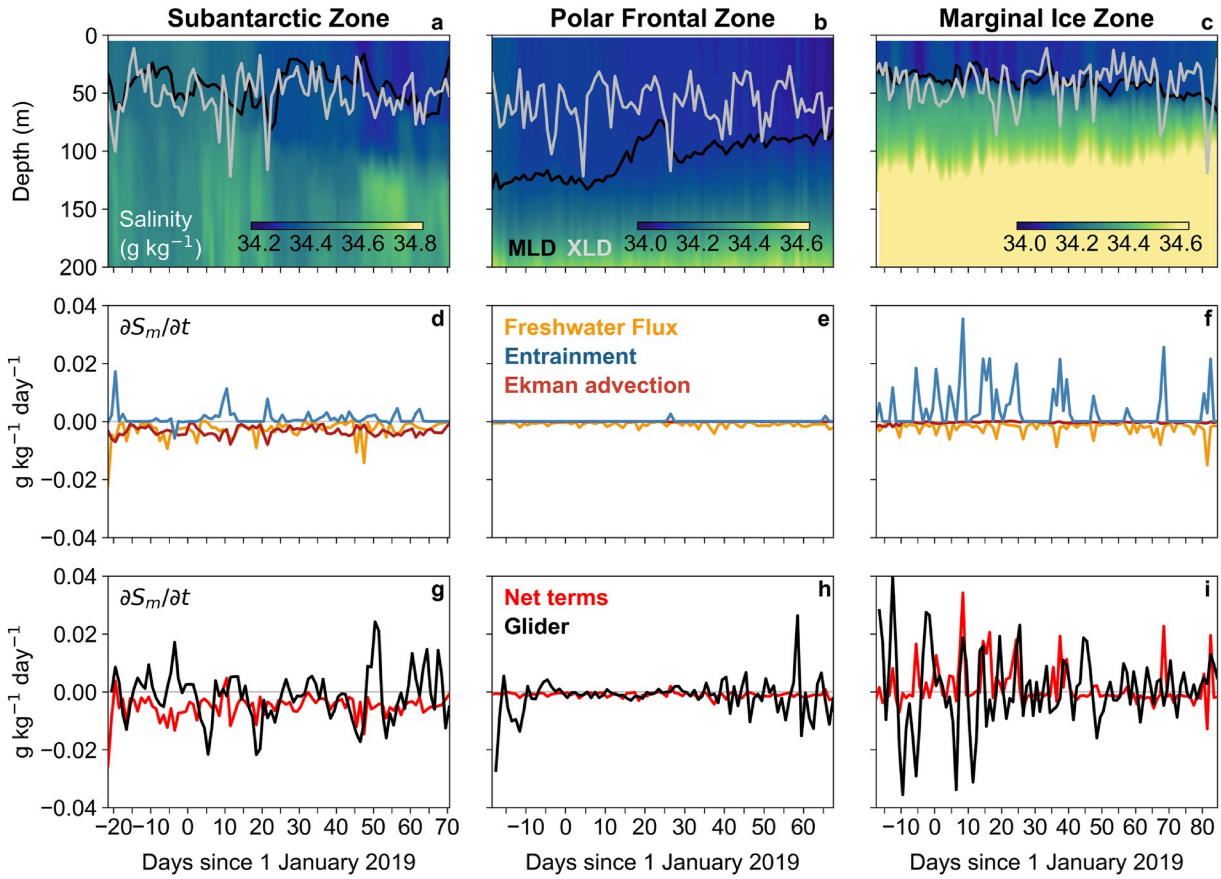

Figure 8. (a–c) Vertical sections of salinity (g kg^{-1}) measured by the gliders for the Subantarctic Zone, Polar Frontal Zone, and Marginal Ice Zone, respectively. Lines indicate the mixed layer depth (MLD; black) and mixing layer depth (gray). Note the colorbar limits vary but are scaled to a range of 0.6 g kg^{-1}. (d–f) Daily S_m change ($\partial S_m/\partial t$, g kg^{-1} day^{-1}) resulting from freshwater flux (orange), entrainment (blue), and Ekman advection (red) as described in Equation 2. (g–i) Red lines indicate the daily S_m change determined from the sum of the budget terms in Equation 2 (lines in d–f), while black line is the observed daily S_m change determined from the glider data in units of g kg^{-1} day^{-1}.

3.3. Salinity

Over the duration of the summer, S_m decreased in the SAZ and PFZ by 0.22 and 0.12 g kg^{-1}, respectively. The mean daily change and standard deviation for these two regions were -0.0013 ± 0.0097 and -0.0016 ± 0.0070 g kg^{-1} day^{-1}. Meanwhile, S_m in the MIZ increased by 0.13 g kg^{-1} at a mean daily rate of 0.0009 ± 0.0139 g kg^{-1} day^{-1} (Figures 8a–8c). The budget terms were unable to reproduce the large variations seen in the observations, showing a near persistent freshening in the SAZ (mean rate of -0.0094 ± 0.0101 g kg^{-1} day^{-1}) and salinity gain in the MIZ (0.0023 ± 0.0095 g kg^{-1} day^{-1}; Figures 8h and 8j). Although individual daily S_m changes determined by the one-dimensional budget analysis in the SAZ did not match up directly with those in the observations, the S_m variance from the daily changes (with the mean and seasonal trend removed) were comparable between the one-dimensional model (1.08×10^{-4} g kg^{-1} day^{-1}) and observations (0.95×10^{-4} g kg^{-1} day^{-1}). For the PFZ and MIZ, the variance of the observations (0.50×10^{-4} and 1.94×10^{-4} g kg^{-1} day^{-1}) were larger than the net terms in the budget (0.01×10^{-4} and 0.95×10^{-4} g kg^{-1} day^{-1}).

We hypothesize that, south of the Polar Front, the mixed layer freshwater lens deposited by the sea-ice melt (Figure 3) behaved as a tracer that was stirred around (Giddy et al., 2021). Therefore, we propose that the poor comparison between the budget and observations was likely due to the abundance of lateral processes, such as isotropic submesoscale flows and stirring of mesoscale salinity gradients. Furthermore, we observed a decrease in the scale of daily S_m changes during late summer, which Giddy et al. (2021) attributed to a seasonal weakening of the submesoscale flows. Assuming S_m changes in Figure 8i were driven by the horizontal stirring of melted sea-ice, the local residence time scale of melted sea-ice was around 2–3 months.

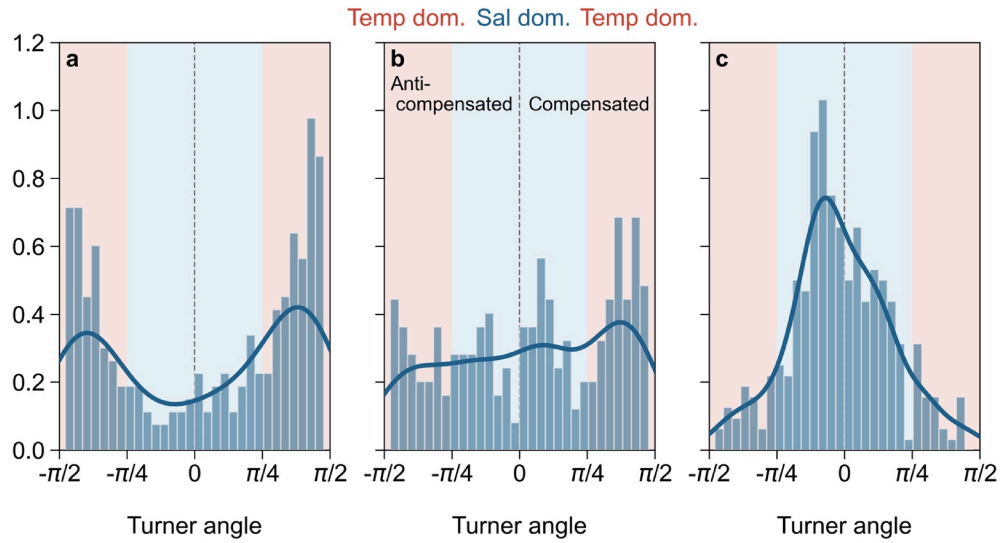

Figure 9. Distribution of the Turner angle (Tu = arctan $\left(\frac{\alpha \Delta T_s}{\beta \Delta S_s}\right)$) for the (a) Subantarctic Zone, (b) Polar Frontal Zone, and (c) Marginal Ice Zone. ΔT_s and ΔS_s represent the 1–10 days variability of mixed layer temperature and salinity determined as T_m and S_m minus their 10-day rolling mean. Tu < 0 indicate where changes in temperature and salinity have the same effect on buoyancy (anticompensated) while Tu > 0 indicate where temperature and salinity compensate in their effect on buoyancy. Red shading highlights where temperature dominates salinity in changes to buoyancy, while blue shading highlights where salinity dominates temperature in changes to buoyancy.

3.4. Relative Roles of Temperature and Salinity on the Intraseasonal Density Variations

We quantified the relative influence of T_m and S_m on the synoptic (1–10 days) variations of density by removing their 10-day rolling means to obtain T_s and S_s, and computed the Turner angle (Turner, 1979)

$$\mathrm{Tu} = \arctan\left(R_\rho\right) \tag{7}$$

using the density ratio (R_ρ), where

$$R_\rho = \frac{\alpha \Delta T_s}{\beta \Delta S_s}. \tag{8}$$

ΔT_s and ΔS_s represent the daily change of T_s and S_s, α is the thermal expansion coefficient and β is the haline contraction coefficient. Both α and β are determined from the in situ temperature and salinity. The density ratio R_ρ was mapped on Tu such that for Tu = $\pi/4$, temperature and salinity variations are fully compensated (i.e., opposite effects on density), while for Tu = $-\pi/4$, temperature and salinity contribute equally to the density variability. The contribution of salinity changes exceeds those from temperature when $-\pi/4 < \mathrm{Tu} < \pi/4$, and temperature changes dominate when $|\mathrm{Tu}| > \pi/4$. Turner angles help to assess the relative importance of temperature and salinity on gradients of density (Rudnick & Martin, 2002; Shroyer et al., 2020; Timmermans & Winsor, 2013). The differences in our Turner angle analysis indicate how daily changes in temperature and salinity impact changes in buoyancy (Figure 9). There was a clear transition in the distribution of Turner angles from a thermal dominated regime in the SAZ to a haline dominated regime in the MIZ. The PFZ was characterized as a transition between the two regimes. In the SAZ, a propensity for anticompensated changes in temperature and salinity were observed, likely representing the interface between the subtropical and polar regimes, where advection of compensating warm/salty and cool/fresh water masses were seen as sharp changes in thermohaline properties on Yearday 22 and 48 in Figures 7a and 8a. In the MIZ, ΔT_s and ΔS_s were primarily anticompensated, revealing the likely dominance of vertical mixing of cold and salty WW into the mixed layer from below.

4. Discussion

We used the presented data to address two main questions: (a) What are the regional contrasts of the intraseasonal variability of mixed layer dynamics, such as depth and stratification? (b) What are the processes that dominate the mixed layer thermohaline variability at intraseasonal time scales across the three regions?

4.1. The Subantarctic Zone

The boundary between the Subtropical and Subantarctic regimes is often considered quasi-continuous and characterized by density-compensating temperature and salinity gradients (Dencausse et al., 2011). Similar to the SAZ glider observations of Swart et al. (2015), our results showed that the summer MLD and stratification was highly variable and was likely responsive to both lateral and temporal processes. Large, though compensating, temperature and salinity gradients were seen to extend below the mixed layer (e.g., Yearday 50, Figure 8a) and led to the largest discrepancies between the budget terms and observed glider variability (Figure 8h). Further, the "mooring mode" sampling pattern of the SAZ glider (Figure 2c) provided confidence that these features were advected into the region rather than the glider crossing frontal gradients. This is also consistent with the findings of Tamsitt et al. (2016), who used output from the Southern Ocean State Estimate model to show that geostrophic heat transport in the Atlantic/Indian section of the ACC can warm the mixed layer by 40% compared to the local heat flux. We note that geostrophic heat transport was not accounted for in our budgets, which may explain discrepancies between the sum of the terms and the observations, particularly in the salinity budget (Faure et al., 2011). Improved estimates of sea surface salinity from satellites or targeted field studies constraining the lateral mesoscale gradient may provide valuable insight into the role of mesoscale advection in the SAZ.

Our observations suggest that heat flux and entrainment were the dominant drivers of the large daily mixed layer temperature variations (>0.1°C day^{-1}; Figures 7h and 7i). Both heat flux and entrainment responded to MLD variability, where the largest mixed layer warming occurred during shallower mixed layers. Deepening of the mixed layer, concurrent with when the mixing layer exceeded the mixed layer, subsequently entrained colder water from below to reduce the mixed layer temperature.

Following Pellichero et al. (2018), we provided an indication for the processes key to water mass transformation by comparing the relative contribution of each term to buoyancy variability. We converted the buoyancy flux for each term to an equivalent heat flux (W m^{-2}) as it represents an intuitive representation of the relative role of each process on buoyancy gain/loss and associated mixed layer variability (Figure 10). Surface heat flux was the largest contributor to the daily mean changes of buoyancy (46%), reflecting the importance of temperature in determining density variations over short time scales in the summer. We find that, despite positive heat fluxes during the summer, entrainment and Ekman advection provided a significant cooling to the surface warming, which together contributed to around half the buoyancy variability induced by heat fluxes (Figure 10). However, due to the density-compensating nature of cooling and freshening by Ekman advection, the mean mixed layer buoyancy change was low in the three regions (-6 ± 5, -25 ± 17, and 3 ± 9 W m^{-2}, respectively). Entrainment induced a large daily mean buoyancy loss (equivalent heat flux of -68 ± 110 W m^{-2}) that provided a non-negligible contribution to the mean summer buoyancy change. As such, the entrainment of colder water from below the mixed layer may provide an important contribution to setting SAMW properties as observed in the Indian Ocean sector of the Southern Ocean in Sallée et al. (2006).

4.2. The Polar Frontal Zone

North of the winter sea-ice maximum, Ekman divergence driven by wind stress curl brings warmer UCDW toward the surface, inhibiting sea-ice formation (Shi et al., 2020). Once at the surface, mixed layer waters are then advected northward and exposed to air-sea interactions where they are transformed into AAIW and SAMW (Abernathey et al., 2016). This northward transport forms part of the overturning circulation and results in over two-thirds of the annual mean surface heat uptake in the PFZ being transported to the northern ACC (Armour et al., 2016). Thus, the PFZ is a critical region for both local heat storage and for heat transport as part of the larger-scale overturning circulation.

Mixed layer buoyancy variations in the PFZ resulted primarily from air-sea fluxes, with buoyancy gain by heat (59%) and freshwater fluxes (22%) accounting for 81% of the total buoyancy variations (Figure 10b). Despite

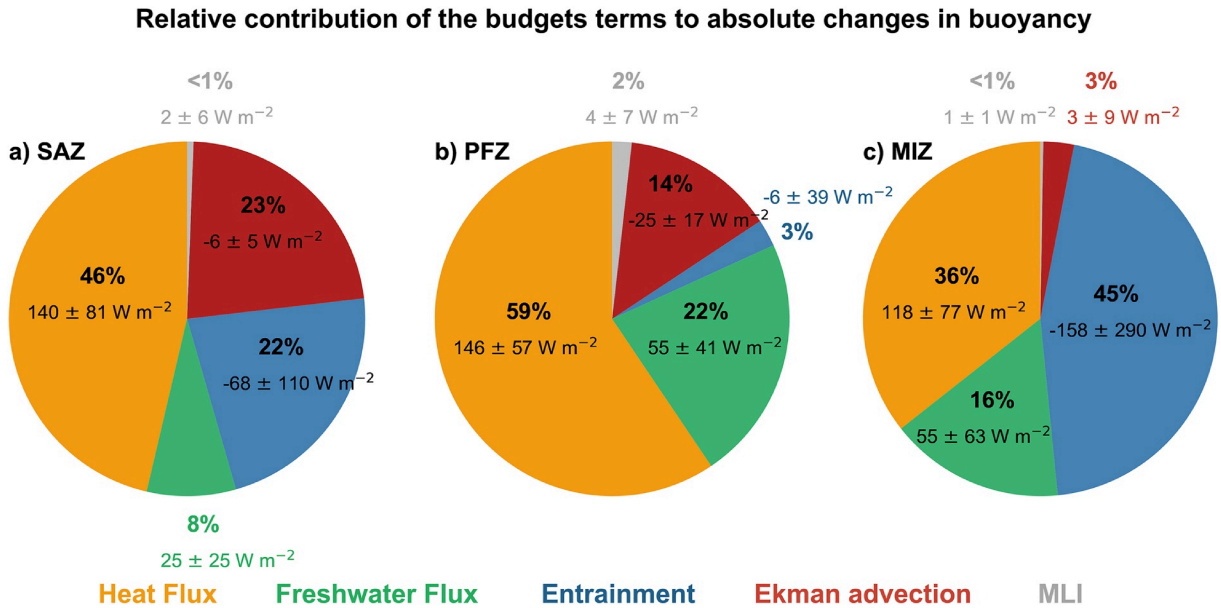

Figure 10. The relative contribution of the individual budget terms in Equations 1 and 2 is shown as a percentage of the total buoyancy flux irrespective of the direction (positive or negative) for the (a) Subantarctic Zone, (b) Polar Frontal Zone, and (c) Marginal Ice Zone. For each term, the mean and standard deviations of their equivalent heat flux (W m^{-2}) are shown to compare their individual contribution to the overall summer mixed layer buoyancy change. The individual terms are heat (orange) and freshwater (green) fluxes, entrainment (blue), and Ekman advection (red), as well as the submesoscale mixed layer instabilities (gray).

similar air-sea fluxes to the SAZ and MIZ throughout the summer, the glider observations showed that the PFZ mixed layer remained comparatively deep and the pycnocline below was weakly stratified (Figure 6b). As a result, the daily magnitudes of mixed layer warming (Figures 7d–7f) and freshening (Figures 8d–8f) that would occur from fluxes alone was lower than both the SAZ and MIZ. This weaker variability may be due to surface heat and freshwater fluxes being distributed over deeper mixed layers. As the PFZ region experienced a higher mean wind stress (0.15 N m^{-2}) when compared to the SAZ (0.12 N m^{-2}) and MIZ (0.09 N m^{-2}), we propose that enhanced wind-driven mixing likely played an important role in keeping the mixed layer deep and the pycnocline weakly stratified. However, other mechanisms such as upwelling induced by Ekman divergence may also contribute to the deeper mixed layers in the PFZ. Further investigation is required to understand this process better.

At the start of summer, the upper bound of UCDW, represented by the 27.3 kg m^{-3} isopycnal (Pellichero et al., 2018), was exposed to the mixed layer (Figure 6b, up to Yearday −14). Throughout the summer, the restratification of the mixed layer led to the formation of lighter density waters, lowering the 27.3 kg m^{-3} isopycnal to beneath the MLD. Thus, progressive buoyancy gain through the summer (i.e., as indicated by the increasing stratification and the shoaling of the MLD in Figure 6b) driven primarily by surface fluxes may also be an important mechanism for reducing the vertical transport of UCDW from the ocean interior to the mixed layer. Our observations showed that the MLD is kept sufficiently deep and close to the XLD throughout summer and infrequently extends below the MLD (Figure 6 and see Figure 2 in Nicholson et al. [2022]). Furthermore, the weak vertical gradients of temperature and salinity below the MLD resulted in entrainment accounting for only 3% of the contribution to the mean buoyancy change, suggesting that the seasonal restratification was effective at suppressing the supply of UCDW to the mixed layer.

Although we did not resolve sea-ice processes in this study, we find large intraseasonal salinity variations during late summer (Figure 8i). Given the proximity of the PFZ study site to the winter maximum sea-ice edge (~120 km) and the time between the start of spring sea-ice melt (10 October 2018, Figure 1) to the first large salinity variation on Yearday 35 (4 February 2019), the advective velocity required for sea-ice meltwater to account for the observed intraseasonal salinity variations is 0.012 m s^{-1}. This is equivalent to the speed of Ekman advection given the mean wind stress over the deployment period and a mixed layer of 100 m. Thus, we propose that sea-ice melt processes occurring further south are most likely only prominent during late summer (February) in the PFZ. During early summer, our budget estimates showed that air-sea freshwater fluxes provided the dominant mechanism for buoyancy gain; however, we observe salinity variations of around 0.015 g kg^{-1} day^{-1}

in the beginning of the time series (e.g., Yearday −11). While these variations may be unaccounted for by the inaccuracies within the reanalysis data (see Section 4.4), it is unlikely due to the deep mixed layers dampening the effects of air-sea fluxes.

4.3. The Marginal Ice Zone

The local sea-ice melt occurred 4 days prior to the deployment of the MIZ glider (Figure 1b). The temporal evolution of under-ice profiles from an Argo float located nearby the MIZ glider (60.45°S, 8.63°W) showed the mixed layer freshened from October to December, which led to a shallower MLD and increased vertical salinity gradient (Figure 3). We propose the primary mechanism that led to this development of the mixed layer was the injection of sea-ice meltwater. However, the shoaling of the deeper pycnocline by about 30 m during late winter suggests that three-dimensional processes may contribute to altering characteristics at the base of and below the mixed layer as well. The freshening of the mixed layer reduced the buoyancy by an amount equivalent to a heat flux of 278 W m^{-2} between 23 October and 13 December. Comparatively, the mean equivalent heat flux from the air-sea fluxes of heat and freshwater flux throughout the summer was 118 and 55 W m^{-2}, respectively. This indicates that the contribution of seasonal mixed layer buoyancy gain likely driven by sea-ice meltwater is an order of 2 and five times that of the mean summertime air-sea fluxes of heat and freshwater, respectively. These observations are consistent with the findings of Abernathey et al. (2016) and Pellichero et al. (2017, 2018) who show that sea-ice meltwater and *E-P* both contribute substantially to the freshwater flux term. However, Pellichero et al. (2017, 2018) grouped precipitation, evaporation, and sea-ice growth/melt into a single freshwater flux term, and so no direct comparison of the relative contribution of sea-ice melt and precipitation can be made. Meanwhile, Abernathey et al. (2016) used circumpolar (south of 50°S), annual averages of water mass transformation from the Southern Ocean State Estimate model to show that *E-P* contributes on average 44% less than sea-ice melt to the total freshwater flux. This is a larger contribution to buoyancy gain by *E-P* than we observed (80% less). However, their study averages over regions further north, where the contribution by *E-P* may be more comparable to sea-ice processes, while our investigation focused over the winter to summer transition and in a region where sea-ice growth and melt strongly dominates over freshwater fluxes.

The newly formed summer mixed layer overlies the cool and salty previous winter mixed layer (Figure 3), which then undergoes surface warming and freshening from air-sea fluxes that approximately double the mean stratification of the upper 100 m from 2.9×10^{-5} s^{-2} on Yearday −12 to 5.2×10^{-5} s^{-2} on Yearday 79 (Figure 6). The dominance of the thermal component in driving buoyancy gain during the post sea-ice melt summer was also observed by Giddy et al. (2021). We showed here that despite increased stratification during summer, mixing below the MLD entrained cooler underlying WW (Figure 7c). This mechanism of vertical mixing is known to introduce heat, salt, carbon, and other properties to the mixed layer, with direct consequences for air-sea heat and carbon exchange (Gordon & Huber, 1990) and formation of sea-ice the following winter (Holland et al., 2014; Stammerjohn et al., 2008). Wintertime entrainment of warmer UCDW into the mixed layer is understood to provide a heat flux of between 20 and 60 W m^{-2}, albeit with large spatial variability (Gordon & Huber, 1990; Pellichero et al., 2017). We found that, during summer, the upward heat flux by entrainment (−54 W m^{-2}) largely balanced out the reported wintertime flux.

4.4. Uncertainty and Limitations of the Study

Our results showed that air-sea heat fluxes and wind-driven mixing were key drivers of mixed layer temperature and salinity variability in the SAZ, PFZ, and MIZ south of Africa. There are, however, several sources of uncertainty, stemming from (a) uncertainty in the reanalysis data sets for atmospheric forcing, (b) the spatiotemporal sampling design of gliders, and (c) the role of lateral processes and those unaccounted for in the mixed layer budget. Below, we discuss how these caveats might influence our conclusions.

4.4.1. Reanalysis Errors

First, we note that all atmospheric reanalyzes are hampered by the relative sparsity of observations in the Southern Ocean, where there is a large spread in their ability to reproduce observed monthly precipitation rates (Boisvert et al., 2020) and turbulent heat fluxes (Liu et al., 2011; Swart et al., 2019). Yu et al. (2019) determined the mean daily differences between observed net surface heat fluxes, from 10 round-trip cruises between Hobart and the Antarctic continent, and four separate reanalysis products. They showed that the reanalysis products

have a mean cooling bias of 8–19 W m^{-2} in the ice-free Southern Ocean. As a result, air-sea heat and freshwater flux terms contribute to the largest source of uncertainty compared to the other mixed layer budget terms (Dong et al., 2007; Pellichero et al., 2017; Ren et al., 2011). ERA5 compares better than other products to observations of momentum (Belmonte Rivas & Stoffelen, 2019; Schmidt et al., 2017), net surface heat flux (Yu et al., 2019), and precipitation (Boisvert et al., 2020) across the Southern Ocean. Nevertheless, to ensure ERA5 is appropriate for our study regions, we performed a sensitivity test to investigate how three commonly used reanalysis products, namely ERA5, JRA55, and MERRA-2 (Figure S2), impacted our mixed layer budget results. The three reanalysis products were applied to the T_m and S_m tendency budgets (Equations 1 and 2), while entrainment and Ekman advection were kept the same, providing three experiments for each region for both T_m and S_m. The root mean square error (RMS) was determined between the glider-observed mixed layer tendencies ($\partial T_m/\partial t$ and $\partial S_m/\partial t$) and the outcome from mixed layer tendency budgets estimated using the three reanalysis products. ERA5 (SAZ) and JRA55 (MIZ) produced the largest RMS for the temperature tendency budget at 0.065°C day^{-1}, while ERA5 (MIZ) produced the largest salinity tendency RMS at 0.0116 g kg^{-1} day^{-1}. However, we find that the interproduct difference between the RMS at each site is an order of magnitude less than the RMS, with the largest difference of 0.006°C day^{-1} between ERA5 and MERRA-2 in the SAZ and 0.0004 g kg^{-1} day^{-1} between ERA5 and JRA55 in the SAZ. This indicates that the mixed layer budget uncertainty is not sensitive to the choice of the reanalysis product.

4.4.2. Glider Sampling Considerations

An important consideration to make when analyzing glider data is how to distinguish between spatial and temporal gradients. This can be understood better by assessing the different sampling strategies of the three gliders. The MIZ glider sampled in such a way as to intentionally capture the submesoscale gradients within a 20 km bow-tie pattern. As such, the day-to-day variability in the observed temperature and salinity is likely a combination of temporal and spatial processes which potentially explain the mismatch of $\partial S_m/\partial t$ between the terms and the observations. To investigate this, we have compared the temperature and salinity profiles between the western and eastern ends of the bow-tie transects and find a propensity for slightly fresher (saltier) mixed layers at the western (eastern) ends of the bow-tie by about 0.02 g kg^{-1} (Figure S4 in Supporting Information S1), which scales with the observed daily salinity changes that the mixed layer budget cannot resolve (Figure 8i). Furthermore, Giddy et al. (2021) used this data set to infer these gradients as stirring of submesoscale flows induced by the seasonal sea-ice melt. We found here that this stirring provided significantly more variability in S_m than air-sea freshwater fluxes over the summer, while episodic entrainment events provided similar daily S_m variations to the stirring of sea-ice induced gradients.

4.4.3. Small-Scale Physics

Discrepancies between the glider-observed thermohaline variations and those described in this study can also be attributed to other nonlinear and turbulent processes such as Langmuir mixing, symmetric instability and ageostrophic submesoscale flows occur at lateral scales of 0.1–10 km (McWilliams, 2016). Mixed layer eddies, which dominate in regions of large lateral buoyancy gradients, have been shown to promote springtime restratification in the Southern Ocean (du Plessis et al., 2017). Conversely, convective mixing by fine-scale cross-frontal advection may be important for mixing, as shown in the SAZ by du Plessis et al. (2019). The potential for restratification to occur by vertical buoyancy fluxes associated with MLIs can be quantified as an overturning stream function based on the strength of the mesoscale lateral buoyancy gradient and the depth of the mixed layer (Fox-Kemper et al., 2008). This stream function can be estimated as an equivalent heat flux following Mahadevan et al. (2012).

We use the lateral buoyancy gradients determined from the lateral motion of the glider (Figure 2) and the MLD to determine the equivalent heat flux potential by MLI (Figure 10). Our results are of similar magnitude to those previously observed in the summer for both the SAZ (du Plessis et al., 2017, 2019) and the MIZ (Giddy et al., 2021), where individual peaks in the equivalent heat flux are of order 10–20 W m^{-2}. The summer mean equivalent heat fluxes (2 ± 6, 4 ± 7, 1 ± 1 W m^{-2} for the SAZ, PFZ, and MIZ, respectively) are comparable to the annual mean 4–10 W m^{-2} proposed by Su et al. (2018) for the Southern Ocean midlatitudes. Compared to the other budget terms, our estimates of the MLI equivalent heat fluxes are negligible (0.3–2%) for all regions (Figure 10). However, one possibility for these weak fluxes is the lack of larger-scale (100–200 km) transects employed by the gliders in the SAZ and PFZ, which prevents us from quantifying the upper ocean mesoscale to submesoscale gradients. Also, submesoscale dynamics are understood to undergo large seasonal cycles and are strongest during winter (Mensa et al., 2013; Sasaki et al., 2017). The growth of MLIs in the MIZ may be

limited to the days following sea-ice melt, which are then rapidly exhausted after the initial restratification (Giddy et al., 2021). In addition, lateral buoyancy gradients measured from glider data are typically underestimated by a factor of $\sqrt{1/2}$ (Thompson et al., 2016) because lateral fronts are very seldom sampled perpendicularly. A better understanding of the role of submesoscale processes requires improved quantification of the lateral buoyancy gradient in future field observation efforts. In terms of symmetric instability, shear production may indirectly induce a vertical buoyancy flux, which may distribute heat vertically from the mixed layer and below; however, we neglect this flux given that symmetric instability is largely slantwise convection and very little turbulence is produced (Buckingham et al., 2019).

4.5. Implications

We have shown that there is a strong regional dependence on the processes that drive intraseasonal variability of mixed layer thermohaline properties. This is a refinement of previous observational studies that consider the Southern Ocean mixed layer temperature and salinity budgets using basin-scale averaging (Dong et al., 2007, 2009; Pellichero et al., 2017; Ren et al., 2011). Surface water mass transformation along the upper limb of the residual overturning circulation is strongly influenced by the northward advection of melted sea-ice (Abernathey et al., 2016). Along its path from the MIZ to the PFZ, the mixed layer density lightens from around $\sigma = 27.4$ kg m^{-3} to $\sigma = 27.3$ kg m^{-3} during summer, encompassing the formation range of AAIW (Figure S3 in Supporting Information S1). The stark contrast of mixed layer stratification and depth between these two regions indicates a regime shift in the processes important for AAIW formation. In the MIZ, vertical mixing is important for reducing the buoyancy gained by surface warming post sea-ice melt. In the PFZ, freshwater fluxes from sea-ice melt and *E-P* are expected to dominate the annual mean buoyancy gain (Abernathey et al., 2016). We showed here that post sea-ice melt, heat fluxes dominate the contribution of freshwater fluxes for summer mixed layer buoyancy gain (Figure 10). However, the late summer arrival of large S_m variations in the PFZ suggests that meltwater transported northward also contributes to the production of less buoyant AAIW (Iudicone et al., 2008; Saenko et al., 2002). This underpins the potential implications for future changes in winter sea-ice extent and volume further south.

Studies suggest that the long-term strengthening of the Southern Hemisphere westerly wind stress is closely related to the positive phase of the Southern Annular Mode (O'Connor et al., 2021; Yang et al., 2007), leading to a poleward shift and increase in wind stress variability linked to storms (Lin et al., 2018). These changes in wind stress are predicted to increase wind-induced upper ocean dissipation, which has been proposed to enhance the vertical mixing across the base of the mixed layer (Munday & Zhai, 2017). Concurrently, there has been an observed increase in the summertime pycnocline stratification and deepening of the MLD across the Southern Ocean (Sallée et al., 2021). We propose that these conditions are likely to be important for mixed layer buoyancy variations by altering entrainment, which we have shown to be an important mechanism for the reduction of WW and potential ventilation of UCDW during summer. Potential implications of reduced entrainment, which may occur due to deeper mixed layers, will likely lead to greater warming of the mixed layer by surface heat flux during the summer, which may reduce the onset of sea-ice formation during the following winter. In contrast, a southward shift and strengthening of Southern Hemisphere storms may reduce summer warming by increasing the vertical mixing across the base of the mixed layer and potentially offset some of the observed changes in stratification.

Unequivocal anthropogenic warming (Gille, 2002, 2008; Hobbs et al., 2020) and freshening (Durack & Wijffels, 2010) of the Southern Ocean has occurred over the past several decades. Warming has occurred primarily north of the ACC, while there has been delayed warming to the south (Armour et al., 2016). This has been attributed to surface heat uptake being balanced by anomalous northward heat transport associated with the wind-driven northward flow. As the SAZ is strongly stratified by temperature (Rintoul & Trull, 2001), we expect upper ocean stratification to be enhanced under increasing surface warming, as shown by Sallée et al. (2021). We find that entrainment provides an important mechanism for summer cooling, which will likely be suppressed under stronger stratification. However, future increases in wind strength have the potential to increase the Ekman transport of cooler waters from further south. The balance between entrainment and Ekman-induced thermohaline changes in a changing climate should be investigated further. To put our study sites into the context of the larger Southern Ocean, we note that the EKE and therefore mesoscale stirring is spatially heterogeneous across the Southern Ocean and is elevated in the lee of major topographic features. Therefore, we expect that submesoscale

variability at our study sites, particularly in the PFZ and MIZ, is likely somewhat moderate compared to other regions such as in the lee of Kerguelen Plateau (Bachman & Klocker, 2020; Rosso et al., 2015), downstream of Shackleton Fracture Zone (Viglione et al., 2018), and the Southwest Indian Ridge (Dove et al., 2021), which all show topographic influence over the spatial distribution of submesoscale variability and fluxes. Therefore, the contribution of air-sea heat and freshwater fluxes to changes in the mixed layer buoyancy are more likely to be larger in our study regions than those impacted by topographical features.

5. Summary

This work provided two nuanced components that build on previous observational work aiming to understand the key drivers of mixed layer temperature and salinity variability in the Southern Ocean by: (a) investigating simultaneous observations of three contrasting regions over the meridional extent of the Southern Ocean and (b) investigating the processes, at daily temporal resolution, that impact mixed layer variability, compared with previous studies which apply larger spatial and temporal averaging. We found that the mixed layer temperature (T_m) and salinity (S_m) varied in direct response to daily forcing by up to 0.2°C day^{-1} and 0.02 g kg^{-1} day^{-1}, with particularly pronounced variability in the SAZ and MIZ. In the SAZ, temperature dominated variations in density, where large variations in the MLD (20–90 m) were linked to large responses (up to 0.3°C day^{-1}) by surface heat fluxes during MLD shoaling phases and entrainment (up to −0.15°C day^{-1}) when the MLD deepened. Meanwhile, persistently deeper MLDs in the PFZ led to lower daily variations of T_m and S_m than the SAZ and MIZ. In the polar regions, sea-ice melt during spring provided a buoyancy gain to the mixed layer at a rate twice that of net surface heat flux and five times that of E-P. Lateral stirring by sea-ice meltwater within the shallow summer mixed layer dominated the temporal haline fluxes, while heat fluxes dominate summer buoyancy gain. Enhanced mixing linked to synoptic storms led to the entrainment of colder winter water into the mixed layer, with scaling estimates suggesting that the entrainment flux in the MIZ is of the same magnitude as the wintertime entrainment of warmer UCDW.

Acknowledgments
This work was supported by the following grants of S. Swart: Wallenberg Academy Fellowship (WAF 2015.0186), Swedish Research Council (VR 2019-04400), STINT-NRF Mobility Grant and NRF-SANAP (SNA170522231782 and SANAP200324510487 with S. Nicholson as PI). S. Swart and M. du Plessis have received funding from the European Union's Horizon 2020 research and innovation program under Grant Agreement 821001 (SO-CHIC) an M. du Plessis was later funded by the European Union's Marie Skłodowska Curie Individual Fellowship under the Horizon 2020 framework with Project ID 101032683. L. Biddle is additionally supported by a Swedish Research Council grant (VR 2020 04281) The authors thank Sea Technology Services (STS), SANAP, the captain, and crew of the S.A. Agulhas II for their field-work/technical assistance. Zach Erickson, Mar Flexas, and Giuliana Viglione (Caltech) contributed to glider piloting throughout the MIZ deployment. The authors thank David Peddie of Offshore Sensing AS for assistance with the Sailbuoy deployment. The authors are grateful to Geoff Shilling and Craig Lee (APL, University of Washington) for hosting the gliders on IOP and the technical advice provided. The authors thank three anonymous reviewers, whose constructive reviews greatly improved this manuscript.

Data Availability Statement

ERA5 data are generated using Copernicus Climate Change Service Information, available online at www.ecmwf.int/en/forecasts/datasets/archive-datasets/reanalysis-datasets/era5. The sea-ice data are made available via http://data.meereisportal.de/data/iup/hdf/s/. The EN4 data are made available via the UK Hadley Met Office at https://www.metoffice.gov.uk/hadobs/en4/download-en4-2-1.html. The ADT data used to determine the fronts are generated by the Archiving, Validation, and Interpretation of Satellite Oceanographic data service of Centre National D'Etudes Spatiales, available online www.aviso.altimetry.fr/en/data/data-access/gridded-data-extraction-tool.html. The code used for this analysis is available at http://doi.org/10.5281/zenodo.5076119 and the data at http://doi.org/10.5281/zenodo.5079763.

References

Abernathey, R. P., Cerovecki, I., Holland, P. R., Newsom, E., Mazloff, M., & Talley, L. D. (2016). Water-mass transformation by sea ice in the upper branch of the Southern Ocean overturning. *Nature Geoscience*, *9*(8), 596–601. https://doi.org/10.1038/ngeo2749

Adams, K. A., Hosegood, P., Taylor, J. R., Sallée, J.-B., Bachman, S., Torres, R., & Stamper, M. (2017). Frontal circulation and submesoscale variability during the formation of a Southern Ocean mesoscale eddy. *Journal of Physical Oceanography*, *47*(7), 1737–1753. https://doi.org/10.1175/jpo-d-16-0266.1

Armour, K. C., Marshall, J., Scott, J. R., Donohoe, A., & Newsom, E. R. (2016). Southern Ocean warming delayed by circumpolar upwelling and equatorward transport. *Nature Geoscience*, *9*(7), 549–554. https://doi.org/10.1038/ngeo2731

Bachman, S. D., & Klocker, A. (2020). Interaction of jets and submesoscale dynamics leads to rapid ocean ventilation. *Journal of Physical Oceanography*, *50*(10), 2873–2883. https://doi.org/10.1175/jpo-d-20-0117.1

Bachman, S. D., Taylor, J., Adams, K., & Hosegood, P. (2017). Mesoscale and submesoscale effects on mixed layer depth in the Southern Ocean. *Journal of Physical Oceanography*, *47*(9), 2173–2188. https://doi.org/10.1175/jpo-d-17-0034.1

Belmonte Rivas, M., & Stoffelen, A. (2019). Characterizing ERA-Interim and ERA5 surface wind biases using ASCAT. *Ocean Science*, *15*(3), 831–852. https://doi.org/10.5194/os-15-831-2019

Biddle, L., & Swart, S. (2020). The observed seasonal cycle of submesoscale processes in the Antarctic Marginal Ice Zone. *Journal of Geophysical Research: Oceans*, *125*, e2019JC015587. https://doi.org/10.1029/2019JC015587

Boccaletti, G., Ferrari, R., & Fox-Kemper, B. (2007). Mixed layer instabilities and restratification. *Journal of Physical Oceanography*, *37*(9), 2228–2250. https://doi.org/10.1175/jpo3101.1

Boisvert, L. N., Webster, M. A., Petty, A. A., Markus, T., Cullather, R. I., & Bromwich, D. H. (2020). Intercomparison of precipitation estimates over the Southern Ocean from atmospheric reanalyses. *Journal of Climate*, *33*(24), 10627–10651. https://doi.org/10.1175/jcli-d-20-0044.1

Brainerd, K. E., & Gregg, M. C. (1995). Surface mixed and mixing layer depths. *Deep Sea Research Part I: Oceanographic Research Papers*, *42*(9), 1521–1543. https://doi.org/10.1016/0967-0637(95)00068-h

Buckingham, C. E., Lucas, N. S., Belcher, S. E., Rippeth, T. P., Grant, A. L., Le Sommer, J., et al. (2019). The contribution of surface and submesoscale processes to turbulence in the open ocean surface boundary layer. *Journal of Advances in Modeling Earth Systems*, *11*(12), 4066–4094. https://doi.org/10.1029/2019MS001801

Carranza, M. M., & Gille, S. T. (2015). Southern Ocean wind-driven entrainment enhances satellite chlorophyll-a through the summer. *Journal of Geophysical Research: Oceans*, *120*, 304–323. https://doi.org/10.1002/2014JC010203

de Boyer Montégut, C., Madec, G., Fischer, A. S., Lazar, A., & Iudicone, D. (2004). Mixed layer depth over the global ocean: An examination of profile data and a profile-based climatology. *Journal of Geophysical Research*, *109*, C12003. https://doi.org/10.1029/2004JC002378

Dencausse, G., Arhan, M., & Speich, S. (2011). Is there a continuous subtropical front south of Africa? *Journal of Geophysical Research*, *116*, C02027. https://doi.org/10.1029/2010JC006587

DeVries, T., & Primeau, F. (2011). Dynamically and observationally constrained estimates of water-mass distributions and ages in the global ocean. *Journal of Physical Oceanography*, *41*(12), 2381–2401. https://doi.org/10.1175/jpo-d-10-05011.1

Dong, S., Garzoli, S. L., & Baringer, M. (2009). An assessment of the seasonal mixed layer salinity budget in the Southern Ocean. *Journal of Geophysical Reseach*, *114*, C12001. https://doi.org/10.1029/2008JC005258

Dong, S., Gille, S. T., & Sprintall, J. (2007). An assessment of the Southern Ocean mixed layer heat budget. *Journal of Climate*, *20*(17), 4425–4442. https://doi.org/10.1175/jcli4259.1

Dong, S., Sprintall, J., Gille, S. T., & Talley, L. (2008). Southern Ocean mixed-layer depth from Argo float profiles. *Journal of Geophysical Research*, *113*, C06013. https://doi.org/10.1029/2006JC004051

Dove, L. A., Thompson, A. F., Balwada, D., & Gray, A. R. (2021). Observational evidence of ventilation hotspots in the Southern Ocean. *Journal of Geophysical Research: Oceans*, *126*, e2021JC017178. https://doi.org/10.1029/2021JC017178

du Plessis, M., Swart, S., Ansorge, I., & Mahadevan, A. (2017). Submesoscale processes promote seasonal restratification in the Subantarctic Ocean. *Journal of Geophysical Research: Oceans*, *122*, 2960–2975. https://doi.org/10.1002/2016JC012494

du Plessis, M., Swart, S., Ansorge, I. J., Mahadevan, A., & Thompson, A. F. (2019). Southern Ocean seasonal restratification delayed by submesoscale wind-front interactions. *Journal of Physical Oceanography*, *49*(4), 1035–1053. https://doi.org/10.1175/jpo-d-18-0136.1

Durack, P. J., & Wijffels, S. E. (2010). Fifty-year trends in global ocean salinities and their relationship to broad-scale warming. *Journal of Climate*, *23*(16), 4342–4362. https://doi.org/10.1175/2010jcli3377.1

Faure, V., Arhan, M., Speich, S., & Gladyshev, S. (2011). Heat budget of the surface mixed layer south of Africa. *Ocean Dynamics*, *61*(10), 1441–1458. https://doi.org/10.1007/s10236-011-0444-1

Forryan, A., Naveira Garabato, A. C., Polzin, K. L., & Waterman, S. (2015). Rapid injection of near-inertial shear into the stratified upper ocean at an Antarctic Circumpolar Current front. *Geophysical Research Letters*, *42*, 3431–3441. https://doi.org/10.1002/2015GL063494

Fox-Kemper, B., Ferrari, R., & Hallberg, R. (2008). Parameterization of mixed layer eddies. Part I: Theory and diagnosis. *Journal of Physical Oceanography*, *38*(6), 1145–1165. https://doi.org/10.1175/2007jpo3792.1

Garau, B., Ruiz, S., Zhang, W. G., Pascual, A., Heslop, E., Kerfoot, J., & Tintoré, J. (2011). Thermal lag correction on Slocum CTD glider data. *Journal of Atmospheric and Oceanic Technology*, *28*(9), 1065–1071. https://doi.org/10.1175/jtech-d-10-05030.1

Giddy, I., Swart, S., du Plessis, M., Thompson, A., & Nicholson, S.-A. (2021). Stirring of sea-ice meltwater enhances submesoscale fronts in the Southern Ocean. *Journal of Geophysical Research: Oceans*, *126*, e2020JC016814. https://doi.org/10.1029/2020JC016814

Gille, S. T. (2002). Warming of the Southern Ocean since the 1950s. *Science*, *295*(5558), 1275–1277. https://doi.org/10.1126/science.1065863

Gille, S. T. (2008). Decadal-scale temperature trends in the Southern Hemisphere Ocean. *Journal of Climate*, *21*(18), 4749–4765. https://doi.org/10.1175/2008jcli2131.1

Good, S. A., Martin, M. J., & Rayner, N. A. (2013). EN4: Quality controlled ocean temperature and salinity profiles and monthly objective analyses with uncertainty estimates. *Journal of Geophysical Research: Oceans*, *118*, 6704–6716. https://doi.org/10.1002/2013JC009067

Gordon, A. L., & Huber, B. A. (1990). Southern Ocean winter mixed layer. *Journal of Geophysical Research*, *95*(C7), 11655–11672. https://doi.org/10.1029/JC095ic07p11655

Gregor, L., Ryan-Keogh, T. J., Nicholson, S.-A., du Plessis, M., Giddy, I., & Swart, S. (2019). GliderTools: A python toolbox for processing underwater glider data. *Frontiers in Marine Science*, *6*, 738. https://doi.org/10.3389/fmars.2019.00738

Hersbach, H., Bell, B., Berrisford, P., Hirahara, S., Horányi, A., Muñoz-Sabater, J., et al. (2020). The ERA5 global reanalysis. *Quarterly Journal of the Royal Meteorological Society*, *146*(730), 1999–2049. https://doi.org/10.1002/qj.3803

Hobbs, W. R., Klekociuk, A. R., & Pan, Y. (2020). Validation of reanalysis Southern Ocean atmosphere trends using sea ice data. *Atmospheric Chemistry and Physics*, *20*(23), 14757–14768. https://doi.org/10.5194/acp-20-14757-2020

Holland, P. R., Bruneau, N., Enright, C., Losch, M., Kurtz, N. T., & Kwok, R. (2014). Modeled trends in Antarctic sea ice thickness. *Journal of Climate*, *27*(10), 3784–3801. https://doi.org/10.1175/jcli-d-13-00301.1

Holte, J., & Talley, L. (2009). A new algorithm for finding mixed layer depths with applications to Argo data and subantarctic mode water formation. *Journal of Atmospheric and Oceanic Technology*, *26*(9), 1920–1939. https://doi.org/10.1175/2009jtecho543.1

Iudicone, D., Madec, G., & Mcdougall, T. J. (2008). Water-mass transformations in a neutral density framework and the key role of light penetration. *Journal of Physical Oceanography*, *38*(7), 1357–1376. https://doi.org/10.1175/2007jpo3464.1

Jouanno, J., Capet, X., Madec, G., Roullet, G., & Klein, P. (2016). Dissipation of the energy imparted by mid-latitude storms in the Southern Ocean. *Ocean Science*, *12*(3), 743–769. https://doi.org/10.5194/os-12-743-2016

Large, W., & Pond, S. (1981). Open ocean momentum flux measurements in moderate to strong winds. *Journal of Physical Oceanography*, *11*(3), 324–336. https://doi.org/10.1175/1520-0485(1981)011<0324:oomfmi>2.0.co;2

Lin, X., Zhai, X., Wang, Z., & Munday, D. R. (2018). Mean, variability, and trend of Southern Ocean wind stress: Role of wind fluctuations. *Journal of Climate*, *31*(9), 3557–3573. https://doi.org/10.1175/jcli-d-17-0481.1

Liu, J., Xiao, T., & Chen, L. (2011). Intercomparisons of air-sea heat fluxes over the Southern Ocean. *Journal of Climate*, *24*(4), 1198–1211. https://doi.org/10.1175/2010jcli3699.1

Mahadevan, A., D'asaro, E., Lee, C., & Perry, M. J. (2012). Eddy-driven stratification initiates north Atlantic spring phytoplankton blooms. *Science*, *337*(6090), 54–58. https://doi.org/10.1126/science.1218740

Marshall, J., & Speer, K. (2012). Closure of the meridional overturning circulation through Southern Ocean upwelling. *Nature Geoscience*, *5*(3), 171–180. https://doi.org/10.1038/ngeo1391

McDougall, T. J., & Barker, P. M. (2011). Getting started with teos-10 and the Gibbs seawater (GSW) oceanographic toolbox. *SCOR/IAPSO WG* (Vol. 127, pp. 1–28).

McWilliams, J. C. (2016). Submesoscale currents in the ocean. *Proceedings of the Royal Society A: Mathematical, Physical and Engineering Sciences*, *472*(2189), 20160117. https://doi.org/10.1098/rspa.2016.0117

Mensa, J. A., Garraffo, Z., Griffa, A., Özgökmen, T. M., Haza, A., & Veneziani, M. (2013). Seasonality of the submesoscale dynamics in the gulf stream region. *Ocean Dynamics*, *63*(8), 923–941. https://doi.org/10.1007/s10236-013-0633-1

Meredith, M., Sommerkorn, M., Cassotta, S., Derksen, C., Ekaykin, A., Hollowed, A., et al. (2019). *Polar regions. Chapter 3, IPCC special report on the ocean and cryosphere in a changing climate*.

Munday, D. R., & Zhai, X. (2017). The impact of atmospheric storminess on the sensitivity of Southern Ocean circulation to wind stress changes. *Ocean Modelling*, *115*, 14–26. https://doi.org/10.1016/j.ocemod.2017.05.005

Nicholson, S.-A., Whitt, D. B., Fer, I., du Plessis, M. D., Lebéhot, A. D., Swart, S., et al. (2022). Storms drive outgassing of CO_2 in the subpolar Southern Ocean. *Nature communications*, *13*(1), 158. https://doi.org/10.1038/s41467-021-27780-w

O'Connor, G. K., Steig, E. J., & Hakim, G. J. (2021). Strengthening southern hemisphere westerlies and Amundsen Sea low deepening over the 20th century revealed by proxy-data assimilation. *Geophysical Research Letters*, *48*, e2021GL095999. https://doi.org/10.1029/2021GL095999

Patoux, J., Yuan, X., & Li, C. (2009). Satellite-based midlatitude cyclone statistics over the Southern Ocean: 1. Scatterometer-derived pressure fields and storm tracking. *Journal of Geophysical Research*, *114*, D04105. https://doi.org/10.1029/2008JD010873

Pellichero, V., Sallée, J.-B., Chapman, C. C., & Downes, S. M. (2018). The Southern Ocean meridional overturning in the sea-ice sector is driven by freshwater fluxes. *Nature Communications*, *9*(1), 1789. https://doi.org/10.1038/s41467-018-04101-2

Pellichero, V., Sallée, J.-B., Schmidtko, S., Roquet, F., & Charrassin, J.-B. (2017). The ocean mixed layer under Southern Ocean sea-ice: Seasonal cycle and forcing. *Journal of Geophysical Research: Oceans*, *122*, 1608–1633. https://doi.org/10.1002/2016JC011970

Pollard, R. T., Rhines, P. B., & Thompson, R. O. (1973). The deepening of the wind-mixed layer. *Geophysical Fluid Dynamics*, *4*(4), 381–404. https://doi.org/10.1080/03091927208236105

Ren, L., Speer, K., & Chassignet, E. P. (2011). The mixed layer salinity budget and sea ice in the Southern Ocean. *Journal of Geophysical Research*, *116*, C08031. https://doi.org/10.1029/2010JC006634

Rintoul, S. R., & Trull, T. W. (2001). Seasonal evolution of the mixed layer in the subantarctic zone south of Australia. *Journal of Geophysical Research*, *106*(C12), 31447–31462. https://doi.org/10.1029/2000JC000329

Rosso, I., Hogg, A. M., Kiss, A. E., & Gayen, B. (2015). Topographic influence on submesoscale dynamics in the Southern Ocean. *Geophysical Research Letters*, *42*, 1139–1147. https://doi.org/10.1002/2014GL062720

Rudnick, D. L., & Martin, J. P. (2002). On the horizontal density ratio in the upper ocean. *Dynamics of Atmospheres and Oceans*, *36*(1–3), 3–21. https://doi.org/10.1016/s0377-0265(02)00022-2

Saenko, O. A., Schmittner, A., & Weaver, A. J. (2002). On the role of wind-driven sea ice motion on ocean ventilation. *Journal of Physical Oceanography*, *32*(12), 3376–3395. https://doi.org/10.1175/1520-0485(2002)032<3376:otrowd>2.0.co;2

Sallée, J.-B. (2018). Southern Ocean warming. *Oceanography*, *31*(2), 52–62. https://doi.org/10.5670/oceanog.2018.215

Sallée, J.-B., Pellichero, V., Akhoudas, C., Pauthenet, E., Vignes, L., Schmidtko, S., et al. (2021). Summertime increases in upper-ocean stratification and mixed-layer depth. *Nature*, *591*(7851), 592–598. https://doi.org/10.1038/s41586-021-03303-x

Sallée, J.-B., Speer, K., Morrow, R., & Lumpkin, R. (2008). An estimate of Lagrangian eddy statistics and diffusion in the mixed layer of the Southern Ocean. *Journal of Marine Research*, *66*(4), 441–463. https://doi.org/10.1357/002224008787157458

Sallée, J.-B., Wienders, N., Speer, K., & Morrow, R. (2006). Formation of subantarctic mode water in the Southeastern Indian Ocean. *Ocean Dynamics*, *56*(5–6), 525–542. https://doi.org/10.1007/s10236-005-0054-x

Sasaki, H., Klein, P., Sasai, Y., & Qiu, B. (2017). Regionality and seasonality of submesoscale and mesoscale turbulence in the North Pacific Ocean. *Ocean Dynamics*, *67*(9), 1195–1216. https://doi.org/10.1007/s10236-017-1083-y

Schmidt, K. M., Swart, S., Reason, C., & Nicholson, S.-A. (2017). Evaluation of satellite and reanalysis wind products with in situ wave glider wind observations in the Southern Ocean. *Journal of Atmospheric and Oceanic Technology*, *34*(12), 2551–2568. https://doi.org/10.1175/jtech-d-17-0079.1

Shi, J.-R., Talley, L. D., Xie, S.-P., Liu, W., & Gille, S. T. (2020). Effects of buoyancy and wind forcing on Southern Ocean climate change. *Journal of Climate*, *33*(23), 10003–10020. https://doi.org/10.1175/jcli-d-19-0877.1

Shroyer, E. L., Gordon, A. L., Jaeger, G. S., Freilich, M., Waterhouse, A. F., Farrar, J. T., et al. (2020). Upper layer thermohaline structure of the Bay of Bengal during the 2013 northeast monsoon. *Deep Sea Research Part II: Topical Studies in Oceanography*, *172*, 104630. https://doi.org/10.1016/j.dsr2.2019.07.018

Spreen, G., Kaleschke, L., & Heygster, G. (2008). Sea ice remote sensing using AMSR-E 89-GHz channels. *Journal of Geophysical Research*, *113*, C02S03. https://doi.org/10.1029/2005JC003384

Stammerjohn, S. E., Martinson, D., Smith, R., Yuan, X., & Rind, D. (2008). Trends in Antarctic annual sea ice retreat and advance and their relation to El Niño–Southern Oscillation and southern annular mode variability. *Journal of Geophysical Research*, *113*, C03S90. https://doi.org/10.1029/2007JC004269

Su, Z., Wang, J., Klein, P., Thompson, A. F., & Menemenlis, D. (2018). Ocean submesoscales as a key component of the global heat budget. *Nature Communications*, *9*(1), 775. https://doi.org/10.1038/s41467-018-02983-w

Swart, S., Chang, N., Fauchereau, N., Joubert, W., Lucas, M., Mtshali, T., et al. (2012). Southern Ocean seasonal cycle experiment 2012: Seasonal scale climate and carbon cycle links. *South African Journal of Science*, *108*(3–4), 11–13. https://doi.org/10.4102/sajs.v108i3/4.1089

Swart, S., du Plessis, M. D., Thompson, A. F., Biddle, L. C., Giddy, I., Linders, T., & Nicholson, S.-A. (2020). Submesoscale fronts in the Antarctic Marginal Ice Zone and their response to wind forcing. *Geophysical Research Letters*, *47*, e2019GL086649. https://doi.org/10.1029/2019GL086649

Swart, S., Gille, S. T., Delille, B., Josey, S., Mazloff, M., Newman, L., et al. (2019). Constraining Southern Ocean air-sea-ice fluxes through enhanced observations. *Frontiers in Marine Science*, *6*, 421. https://doi.org/10.3389/fmars.2019.00421

Swart, S., Speich, S., Ansorge, I. J., & Lutjeharms, J. R. (2010). An altimetry-based gravest empirical mode south of Africa: 1. Development and validation. *Journal of Geophysical Research*, *115*, C03002. https://doi.org/10.1029/2009JC005299

Swart, S., Thomalla, S. J., & Monteiro, P. (2015). The seasonal cycle of mixed layer dynamics and phytoplankton biomass in the sub-Antarctic zone: A high-resolution glider experiment. *Journal of Marine Systems*, *147*, 103–115. https://doi.org/10.1016/j.jmarsys.2014.06.002

Tamsitt, V., Cerovečki, I., Josey, S. A., Gille, S. T., & Schulz, E. (2020). Mooring observations of air-sea heat fluxes in two subantarctic mode water formation regions. *Journal of Climate*, *33*(7), 2757–2777. https://doi.org/10.1175/jcli-d-19-0653.1

Tamsitt, V., Talley, L. D., Mazloff, M. R., & Cerovečki, I. (2016). Zonal variations in the Southern Ocean heat budget. *Journal of Climate*, *29*(18), 6563–6579. https://doi.org/10.1175/jcli-d-15-0630.1

Thompson, A. F., Lazar, A., Buckingham, C., Naveira Garabato, A. C., Damerell, G. M., & Heywood, K. J. (2016). Open-ocean submesoscale motions: A full seasonal cycle of mixed layer instabilities from gliders. *Journal of Physical Oceanography*, *46*(4), 1285–1307. https://doi.org/10.1175/jpo-d-15-0170.1

Timmermans, M.-L., & Winsor, P. (2013). Scales of horizontal density structure in the Chukchi Sea surface layer. *Continental Shelf Research*, *52*, 39–45. https://doi.org/10.1016/j.csr.2012.10.015

Turner, J. S. (1979). *Buoyancy effects in fluids*. Cambridge University Press.

Viglione, G. A., Thompson, A. F., Flexas, M. M., Sprintall, J., & Swart, S. (2018). Abrupt transitions in submesoscale structure in southern drake passage: Glider observations and model results. *Journal of Physical Oceanography*, *48*(9), 2011–2027. https://doi.org/10.1175/jpo-d-17-0192.1

Villas Bôas, A., Sato, O., Chaigneau, A., & Castelão, G. (2015). The signature of mesoscale eddies on the air-sea turbulent heat fluxes in the South Atlantic Ocean. *Geophysical Research Letters*, *42*, 1856–1862. https://doi.org/10.1002/2015GL063105

Vivier, F., Iudicone, D., Busdraghi, F., & Park, Y.-H. (2010). Dynamics of sea-surface temperature anomalies in the Southern Ocean diagnosed from a 2D mixed-layer model. *Climate dynamics*, *34*(2–3), 153–184. https://doi.org/10.1007/s00382-009-0724-3

Whitt, D. B., Nicholson, S., & Carranza, M. (2019). Global impacts of subseasonal (<60 day) wind variability on ocean surface stress, buoyancy flux, and mixed layer depth. *Journal of Geophysical Research: Oceans*, *124*, 8798–8831. https://doi.org/10.1029/2019JC015166

Whitt, D. B., & Taylor, J. R. (2017). Energetic submesoscales maintain strong mixed layer stratification during an autumn storm. *Journal of Physical Oceanography*, *47*(10), 2419–2427. https://doi.org/10.1175/jpo-d-17-0130.1

Yang, X.-Y., Wang, D., Wang, J., & Huang, R. X. (2007). Connection between the decadal variability in the Southern Ocean circulation and the southern annular mode. *Geophysical Research Letters*, *34*, L16604. https://doi.org/10.1029/2007GL030526

Yu, L., Jin, X., & Schulz, E. W. (2019). Surface heat budget in the Southern Ocean from 42°S to the Antarctic Marginal Ice Zone: Four atmospheric reanalyses versus icebreaker aurora australis measurements. *Polar Research*, *38*. https://doi.org/10.33265/polar.v38.3349

Yuan, X., Patoux, J., & Li, C. (2009). Satellite-based midlatitude cyclone statistics over the Southern Ocean: 2. Tracks and surface fluxes. *Journal of Geophysical Research*, *114*, D04106. https://doi.org/10.1029/2008JD010874